Promising Bending Properties of a New As-Rolled Medium-Carbon Steel Achieved with Furnace-Cooled Bainitic Microstructures

Vahid Javaheri[1*], Sakari Pallaspuro[1], Antti Kaijalainen[1], Saeed Sadeghpour[1], Jukka Kömi[1], David Porter[1]

[1]Centre for Advanced Steels Research, Materials and Mechanical Engineering, University of Oulu, P.O. Box 4200, 90014 Oulu, Finland

Abstract:

The bending properties of a new thermomechanically processed medium-carbon (0.40 wt.% C) low-alloy steel, intended for the slurry transportation pipeline application, have been investigated. The studied material was hot-rolled to 10 mm thick strips followed by direct quenching to two different quench-stop temperatures (QST) of 560 °C and 420 °C. The samples were subsequently cooled slowly to room temperature in a furnace, producing two different bainitic microstructures. In general, the final microstructures on the centerline consisted of different bainitic features with yield strengths of a ~700 MPa and ~1200 MPa for QST 560 °C and 420 °C, respectively. To determine the factors affecting bendability, as determined by three-point brake press bending tests, local microstructural features and texture were characterized with transmission and scanning electron-microscopy and macrohardness tests. Detailed quantitative microstructural evaluation of both subsurface and mid-thickness regions revealed that the bainitic sample produced at the higher temperature (QST 560) consisted of almost equal amounts of bainite types B1 and B2, where B1 has bainitic sheaves with a low dislocation density and intralath cementite, and B2 a very dislocation-dense morphology with mainly interlath cementite. In the QST 420 sample, the high dislocation density components B2 bainite and martensite were dominant, although martensite was only present near the strip surfaces. Different post-rolling cooling conditions did not change the general crystallographic theme but resulted in a slight increase in the texture intensity of the QST 420 sample. Neither the concave nor convex subsurface regions showed significant changes in texture after bending. The more favorable distributions of microstructural components and textural component intensities in the QST 560 sample resulted in higher elongation to fracture and work-hardening capacity, resulting a smaller minimum usable punch radius than for the stronger QST 420 sample. Fractographic examination of the cracked surfaces revealed that cracks developed by shear band formation followed by surface roughening, which promoted subsequent void and microcrack nucleation and growth.

Keywords: Bendability, Furnace-cooled bainite, Medium-carbon steel, Fractography, Image quality analysis, Texture.

1. Introduction

When designing a new steel grade for long-distance transportation of slurry or cement by pipelines system, besides excellent wear resistance to meet the harsh working conditions, an optimal balance of all mechanical properties such as strength, hardness and toughness is required. However, from a pipe fabrication viewpoint, also formability is a key parameter, considering the common production route of cold forming the strips to a pipe shape and then welding the edges followed with the final hardening treatment especially in the case of pipe with the smaller diameter or with an uncommon shape like elbows . Generally, high strength and hardness are only possible at the expense of formability and toughness, but the overall balance depends on the details of the microstructures involved. Particularly in the case of the complex microstructures of medium-carbon steels, it is challenging to properly design, characterize and quantitatively analyze the microstructural details.

Tensile testing is the most common way to experimentally measure strength and ductility of materials. However, determining formability via tensile tests is inadequate to predict surface crack formation and failure in bending [1]. Hence, to measure the ability of a material to withstand bending without any serious damage (bendability) and to evaluate the resistance to crack nucleation and growth, bending tests are usually performed along with tensile testing for a more precise evaluation of the forming capability. Bendability is related to the sheet bulk mechanical properties as well as to microstructural features [2]. Several systematic studies have been concerned with the effect of microstructural characteristics and textural aspects on bending properties, especially in the case of direct-quenched martensitic sheet steels [1,3–7]. Take apart of homogenization and refinement of the microstructure which has been widely reported as the main factor influencing the bending properties [8], Saastamoinen et al. [9,10] demonstrated that bendability of direct-quenched steels mainly depends on crystallographic texture, dislocation density and size and distribution of second phase e.g. carbides in the microstructure. They improved the bendability of a martensitic direct-quenched low-alloy strip steel by reducing the subsurface dislocation density and hardness as well as reducing the carbides size through the microstructure, applying a tempering treatment at around 600°C. Roumina et. al [11], by testing the bendability of a compositionally-graded martensitic steel, showed that introducing more ductile phase at the surface area can improve the bending properties thanks to suppression of cracks propagation. However, it has been found [8,12–14] that during deformation and mechanical deformation, transformation of retained austenite to the martensite, especially large austenite islands which are less stable due to lower content of carbon compared to the small islands, can influence the initiation of voids and subsequent microcracks formation.

Moreover, orientational dependence of mechanical properties, especially Charpy impact and bending properties has been largely reported both in the past and more recently [3,7,15–17]. For instant, it has been observed that formation of typical alpha fiber during hot rolling could have a unfavorable effect on bending properties [17] and can be also associated with the planar anisotropy in direct quenched steels [18]. However, the role of specific crystallographic orientations which are/are not in favor of bending failure and damage is

not well stablished yet. In addition, correlation of individual microstructural components in a complicated microstructure like a medium-carbon bainitic microstructure with various bainitic morphologies has not been studied yet.

Thus, in the present work, the failure mode and damage development under three-point bending conditions were studied for two hot-rolled, step-quenched and furnaced cooled bainitic microstructures of a newly designed low-alloy medium-carbon steel. Apart from the conventional characterization of bending damage using visual inspection and in order to provide a failure development guideline, damaged and fracture surfaces were precisely investigated by microscopic examinations. In addition, the correlation between bendability and the microstructural and crystallographic characteristics were studied mainly using orientational distribution function (ODF) maps and image qualities obtained from the EBSD data. In particular, the role of specific crystalline orientations and microstructural components on the crack initiation and growth during bending were discussed.

2. Experimental methodology

2.1. Test material

The material used in this work was designed and manufactured in the laboratory using a steel with the nominal composition of 0.40 C, 0.15 Si, 0.25 Mn, 0.90 Cr, 0.50 Mo and 0.012 Nb (wt.%). After casting and laboratory hot-rolling, the sheet materials with a finish rolling temperature of 800 °C, which is slightly above A_3, were subjected to direct-quenching by immersion in water to quench-stop temperatures (QST) of either 560 °C (upper bainite formation region) or 420 °C (lower bainite formation region). This was immediately followed by very slow cooling in a furnace pre-set to the related QST to produce different bainitic microstructures. The idea with such a treatment was to roughly simulate industrial hot strip rolling, direct quenching and coiling. The hot-rolling process was performed in two stages (Fig. 1): a 4-pass rough rolling above the recrystallization stop temperature (RST) in the temperature window of 1200–1100 °C with a total reduction of 48 % followed by a 4-pass finish rolling stage below RST in the temperature range of 950–800 °C with a total reduction of 32 %. Temperature was recorded during the whole process using a thermocouple, which was inserted in the center of each block before rolling. QSTs were selected based on the upper and lower bainite formation regions determined from dilatometry results and Time-Temperature-Transformation (TTT) diagram, which are presented in Ref. [19]. In this way, two as-rolled samples with the same composition and the same hot rolling treatment but different post-rolling cooling paths and final microstructures were used in this study. More details about the material composition and as-rolled properties can be found elsewhere [19,20].

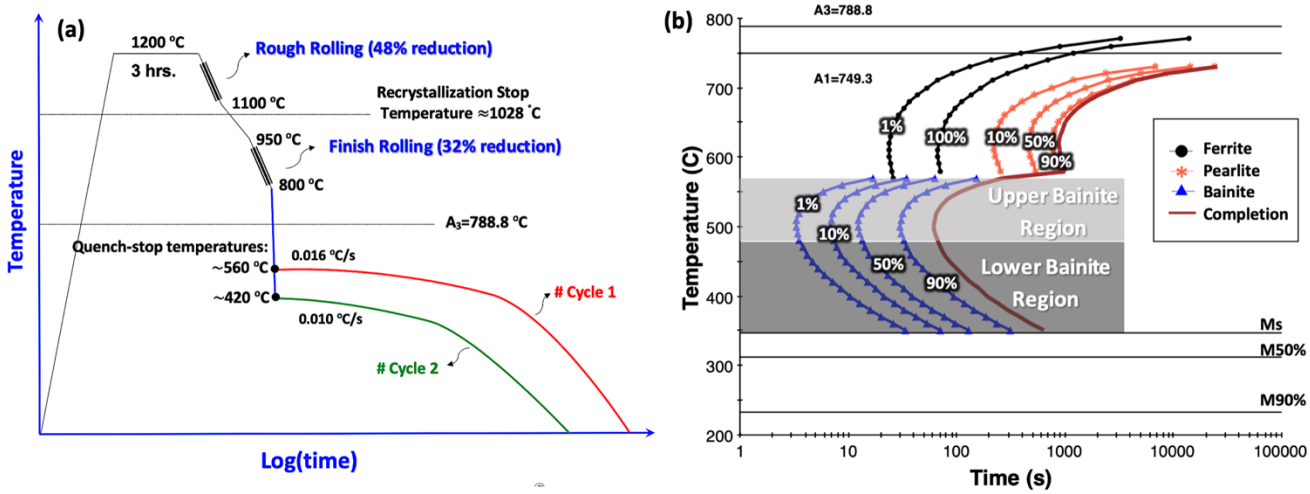

Figure 1. a) Schematic presentation of thermomechanical rolling process along the subsequent cooling paths along with b) the Time-Temperature-Transformation (TTT) diagram for the studied material.

2.2. Mechanical properties

To evaluate the bendability of the samples, three-point bending tests were carried out at room temperature with cylindrical punches in an Ursviken Optima 100 bending machine as shown schematically in Fig. 2(a). Plate specimens, having a thickness (t) of 10 mm, width (w) of 100 mm and length (L) of 170 mm, were bent with a bending angle of 90° and the bend axis (BA) parallel to the transverse direction (BA‖TD). Both longitudinal edges were in the as-rolled condition (no cutting parallel to the rolling direction, no grinding). The die opening width (W) was 100 mm and the punch radius (R) varied from 15 mm to 35 mm. After the tests, the quality of the bent surface was inspected visually to determine the bendability by classifying the defects and determining the minimum bending radius that produces a defect free bend. Slight surface waviness did not lead to rejection in visual inspection. However, if any small surface or edge cracks, large dents, or any other severe surface defects appeared, the bend result was considered as failed. It should be noted that the limited quantities of the laboratory-scale test materials did not permit a full, statistical analysis of the repeatability of the results.

Macrohardness was measured using a Duramin-A300 (Struers) tester under a 100 N load. The as-rolled hardness was determined as a mean value of ten measurements on the cross-section containing the rolling direction (RD) and normal direction (ND). Through-thickness hardness profiles of the bent samples were taken on the RD-ND cross-section where the distance between each measurement was 1 mm.

Three parallel tensile tests for each material were carried out at room temperature in accordance with the European standard EN 10002 using a stain rate of 0.008 s^{-1}. The round specimens cut and machined from the mid-thickness of as-rolled samples with their longitudinal axis parallel to the RD. The samples with a diameter of 6 mm and gage length of 30 mm were prepared in accordance with the ASTM E8M standard for the sub-size samples.

2.3. Microstructural Characterization

After the standard metallographic sample preparation, microstructural features of the polished samples were analyzed using a light microscope and a laser scanning confocal microscope (VK-X200, Keyence Ltd.), and also a Sigma Zeiss field-emission scanning electron microscope (FESEM) equipped with electron backscatter diffraction (EBSD). 2% Nital etchant was used when needed. Due to the complexity of the microstructures, beside the FESEM images, also EBSD image quality was used to detect and to quantify the microstructural components. Microstructural constituents with varying intrinsic dislocation density and surface topology give consequently different IQ values in EBSD measurements [21]. Hence, IQ data can be numerically analyzed to give a quantitative characterization of microstructure. For this purpose, normalized IQ histograms were deconvoluted into multiple peaks with a normal distribution shape on the basis of previous work by DeArdo [22,23]. Then, each peak was attributed to a specific morphology based on the location of the peak, i.e. the mean IQ value and the ratio of the area under each peak to the total normalized IQ area were considered to give the fraction of each microstructural constituent. More detailed microstructural characterization was performed via higher resolution microscopy employing a 200-kV energy filtered scanning transmission electron microscope (JEOL JEM-2200FS EFTEM/STEM). 3 mm diameter transmission electron microscopy samples were cut and punched from the mid-thickness of as-rolled samples. They were ground to initially to 0.1 mm thick wafers and then further ground down to approximately 0.08 mm. Finally, samples were electro-polished at 25 V in an electrolyte consisting of perchloric acid, butyl cellosolve, distillated water and ethanol.

Microtextural characterization was performed using EBSD mappings, which were recorded under an accelerating voltage of 15 kV, a working distance of 15 mm and step size of 0.2 μm. The scanned field size was about 200 x 200 μm^2. Several EBSD runs were carried out on different samples and locations to evaluate the texture and microstructural non-homogeneity across the thickness. A schematic specimen location map is shown in Fig. 2(b-c) to illustrate the sample positions and their relative areas. The FESEM was also used for a fractographic study of crack initiation and propagation from the untouched fracture surfaces, and EBSD scans were made on polished cross-sections across cracked regions.

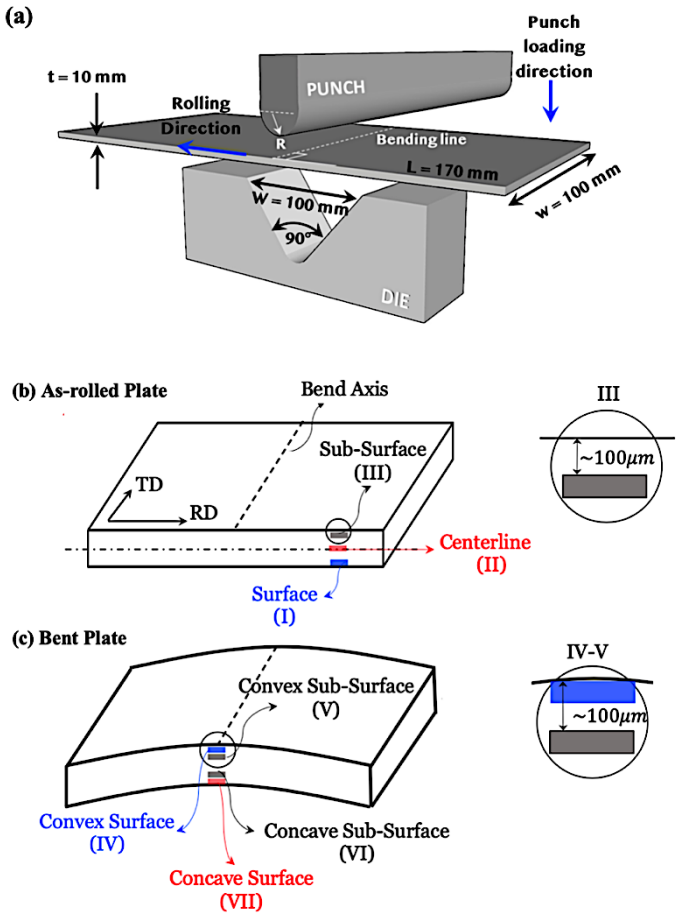

Figure 2. a) Schematic illustration of the three-point bending test setup along with the test specimen dimensions. b) Sample locations for FESEM and EBSD measurements in as-rolled material (positions I-III). c) Sample locations for FESEM and EBSD measurements in undamaged bent samples (positions IV-VII).

3. Results and Discussion

3.1. Microstructures of the rolled material

The starting microstructure of as-rolled samples mainly consisted of very fine lath-like and plate-like bainitic sheaves which were distributed within the severely deformed and elongated prior austenite grains. In addition, there was a significant amount of elongated ferrite and carbon enriched martensite/austenite (M/A) islands below the rolled surfaces down to a depth of 100-150 μm as shown for example in Fig. 3. Due to the low finish rolling temperatures used, ferrite can form near the surfaces during hot-rolling as a result of decarburization during slab heating at 1200 °C and subsequent natural cooling during rolling passes. The formation of ferrite leads to rejection of carbon to the austenite and martensite formation during subsequent quenching. The microstructure of the QST 560 sample was almost the same as that of the QST 420 material and, for the sake of brevity, only the results for the QST 420 sample are presented here. More results and discussions will be presented later on the subsurface and centerline regions for both samples.

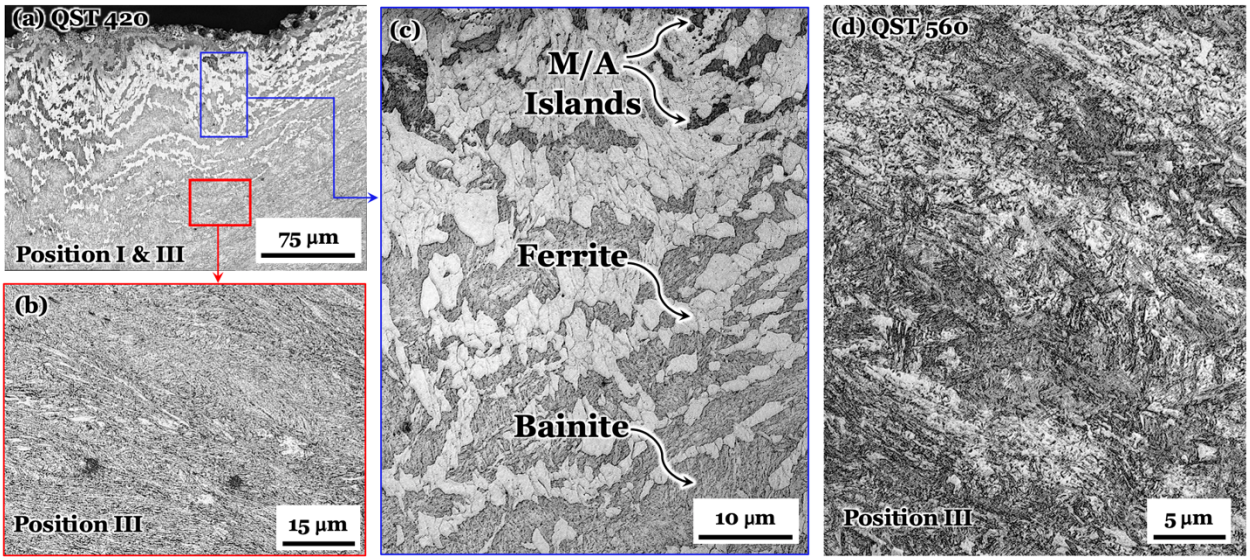

Figure 3. a) Optical micrograph of QST 420 from the surface and subsurface regions along with higher magnifications of highlighted (red and blue) regions b) subsurface and c) surface.

TEM investigations revealed two main types of bainitic morphologies in both samples. Bainitic sheaves composed of a matrix of bainitic ferrite laths with very low dislocation density separated by intralath cementite, as shown in Fig. 4(a-b), which is here referred to as bainite type B1. A second morphology (B2) comprised bainitic sheaves with interlath cementite precipitates (Fig. 4(c-d)). Despite of the formation of cementite within the bainite platelets, the main characteristic of this morphology was the presence of a high density of dislocation networks inside the ferritic laths as shown in Fig. 4(d). Similar observation of such tangled high-density dislocation networks pinned with very fine precipitates in the lath bainite structures has been reported previously by Thao [24]. Although cementite distribution in the B1 morphology was very similar to that of upper bainite and in B2 was very similar to that of lower bainite structure in Bhadeshia's bainite classification system [25], here, the terms B1 and B2 were used as their later quantitative analysis was based on EBSD-IQ data, which is mainly related to the dislocation density of the microstructural component and not the cementite distribution. As regards, terms of upper bainite and lower bainite have not been used directly for the sake of accuracy.

Although dislocation density is mainly a result of the temperature at which the bainitic ferrite forms, precipitates can also stabilize the dislocation networks. During bainite formation at higher temperature, excess carbon from the supersaturated bainitic plate can diffuse to the residual austenite, which leads eventually to formation of intralath cementite resulting in a weak network of dislocations inside the ferritic bainitic plates. When the transformation temperature is low, carbon can partition only partially to the residual austenite. Remaining carbon can precipitate in ferritic bainite laths as interlath cementite, which increases crystal defects and dislocations stability. Fig.4(e) presents the selected area diffraction (SAD) pattern obtained from the highlighted area in Fig.4(b) along with cementite indexing of the SAD pattern, which is in agreement with the earlier reported orientation relationship between the matrix ferrite and one of the cementite variants [26] indicating formation of intralath cementite.

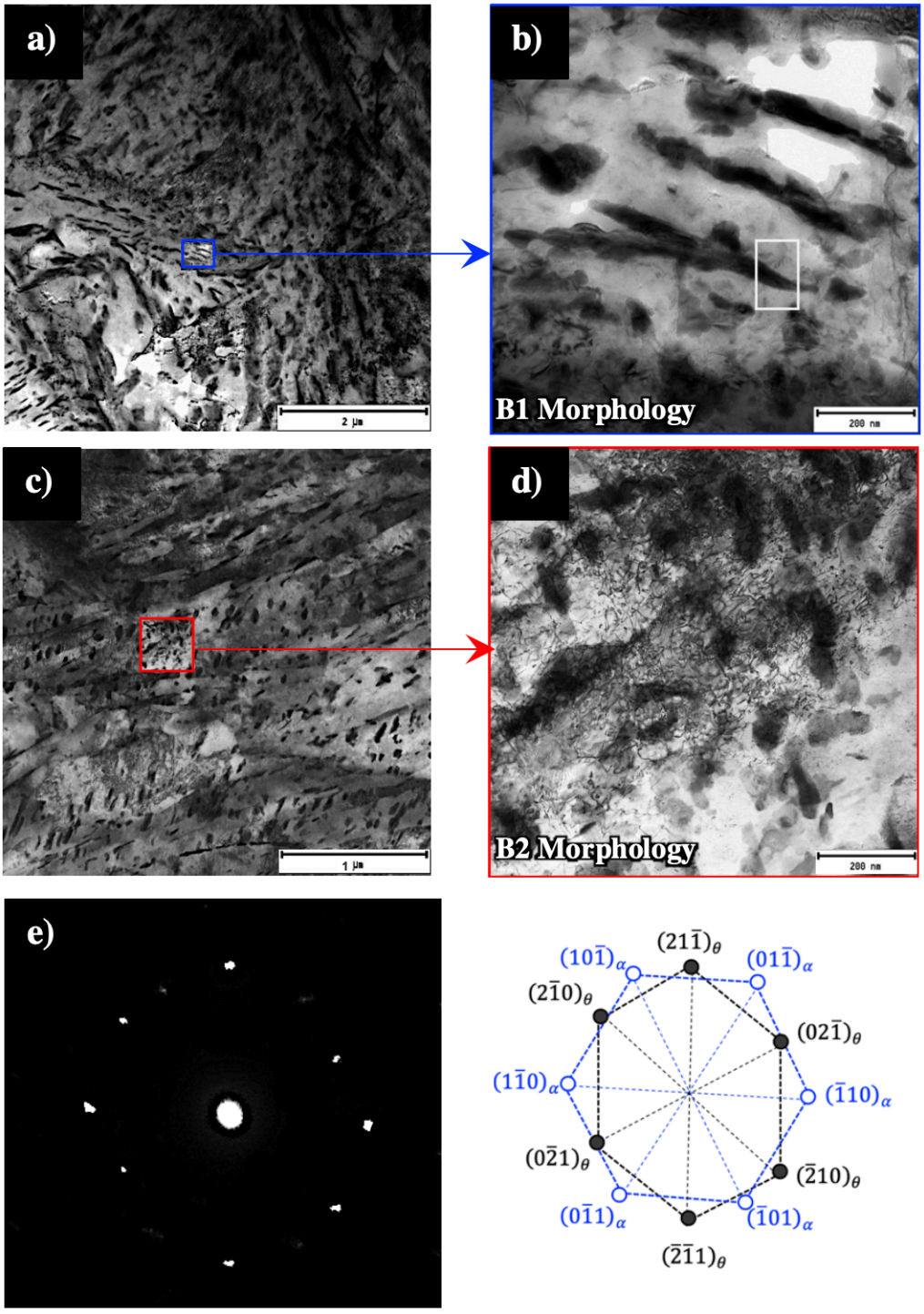

Figure 4. Bright field STEM image of transformed products of studied samples after furnace cooling. Two different magnifications: a-b) indicate cementite precipitation between the ferritic bainitic laths containing a few dislocation networks, c-d) cementite present within the ferritic bainitic plates containing a dense network of dislocations, e) indexed SAD pattern for the bainitic ferrite matrix and cementite obtained from the highlighted area in Fig. 4(b).

In order to quantify the fraction of each microstructural constituents, especially B1 and B2 types of bainite, the EBSD-IQ values were analyzed based on the method developed by DeArdo [22] using MATLAB software. As explained previously [21], pattern or image quality (IQ) which is one of the important maps constructed from the EBSD data describes the quality of acquired diffraction patterns and can often reveal more structural features

than an secondary electron image. Generally, different factors can cause contrast variation in an IQ image for example microstructural morphologies, phase characteristics, surface topology, local chemistry and/or other features of the microstructure like residual plastic deformation left from the sample preparation [27,28]. However, the experiments shows [21,28] an IQ value depends mainly on the amount of strain in the crystal lattice, i.e. mainly on given dislocation density, so that a microstructure component with a high dislocation density yields a low IQ value. In general, during phase transformations under continuous cooling, the IQ value of the transformed microstructural components decreases as the transformation temperature drops through the sequence (polygonal) ferrite, upper bainite, lower bainite, martensite. According to the previous works [22,29], the location of each deconvoluted peak related to each morphology in the normalized IQ axis (from 0 to 100) were considered as follows: (Polygonal) ferrite ~70-80, bainite type B1 ~50-70, bainite type B2 ~30-40 and martensite ~20-30. The EBSD image quality obtained from the subsurface of QST 420 and QST 560 samples are presented in Fig. 5 and Fig. 6, respectively. QST 420 contained about 4.5 % (polygonal) ferrite, 19.5 % B1 bainite (bainite with low dislocation density), 52 % B2 bainite (bainite with high dislocation density) and 24 % martensite including M/A islands (Fig. 5(d)). As the thermocouple was located at the center of rolled plate and martensite start temperature (Ms) for the studied material is about 350 °C, the high subsurface fraction of martensite in the QST 420 sample is probably due to the surface temperature dropping below Ms during quenching as QST for this sample was near the Ms temperature.

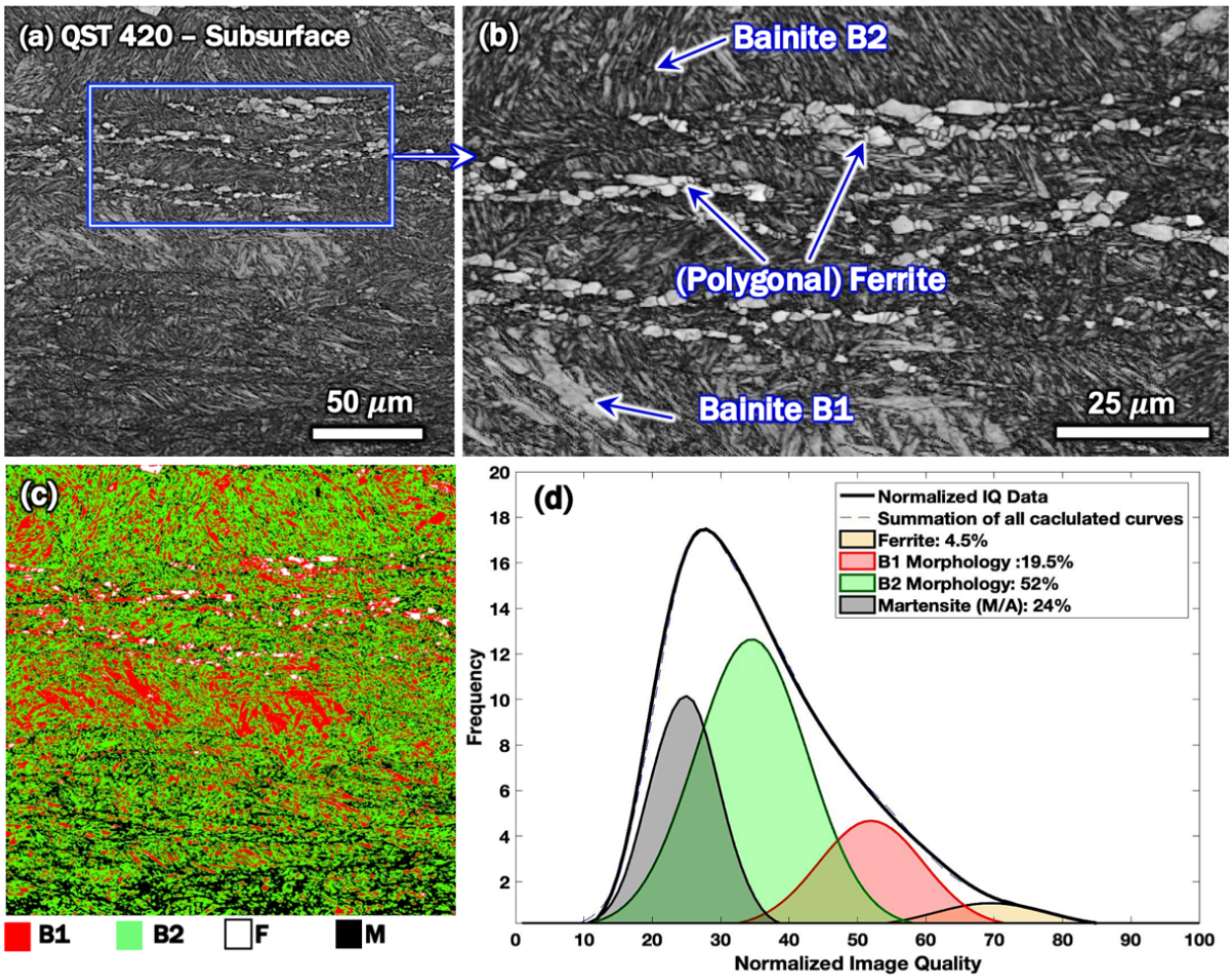

Figure 5. QST 420 subsurface on RD-ND section (Position III): a) and b) EBSD image quality, c) location map of identified microstructural components based on their IQ values and d) IQ distribution and fraction of each microstructural component.

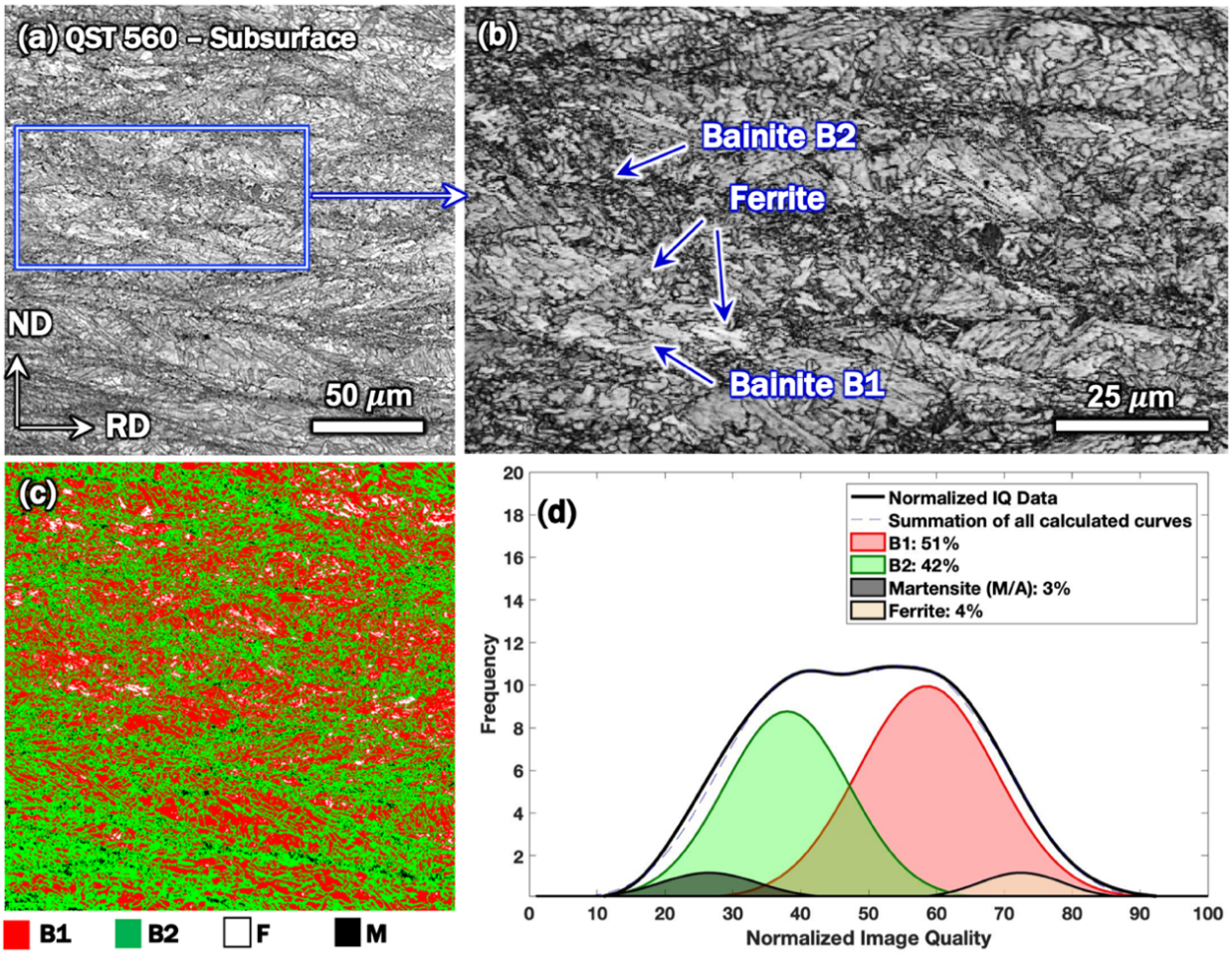

Figure 6. QST 560 subsurface on RD-ND section (Position III): a) and b) EBSD image quality, c) location map of identified microstructural components based on their IQ values and d) IQ distribution and fraction of each microstructural component.

According to Fig. 6(d), the subsurface microstructure of the QST 560 sample consisted of about 4 % ferrite (F), 51% B1 bainite, 42 % B2 bainite and 3 % martensite. The location of each identified microstructural components based on their IQ value has been highlighted in different colors in the image quality maps, see Figs. 5(c) and 6(c).

The image quality of the centerline of both samples were analyzed in the same way. The IQ images along with the location of each identified component and IQ graphs are presented in Fig. 7. The microstructure of QST 420 sample was composed of mainly bainite B2 (75%) where the rest of microstructure was B1 (25%), formed within the elongated prior austenite grains. Unlike the subsurface of the QST 420 sample, no sign of martensite formation was found in centerline microstructure. The QST 560 consisted of equal amount of B1 and B2 morphologies. In QST 560, which has the higher transformation temperature of the two treatments, bainite type B1 forms first making the residual austenite richer in carbon, and thereby increasing the tendency of B2 type formation such that final microstructure was a mixture of B1 and B2 with an almost equal share. On the other hand, as the transformation temperature of QST 420 is low and diffusion is slow, a large amount of carbon is trapped in the ferritic bainite and cannot diffuse to the austenite, which leads to the formation of a significant amount of interlath cementite in the microstructure.

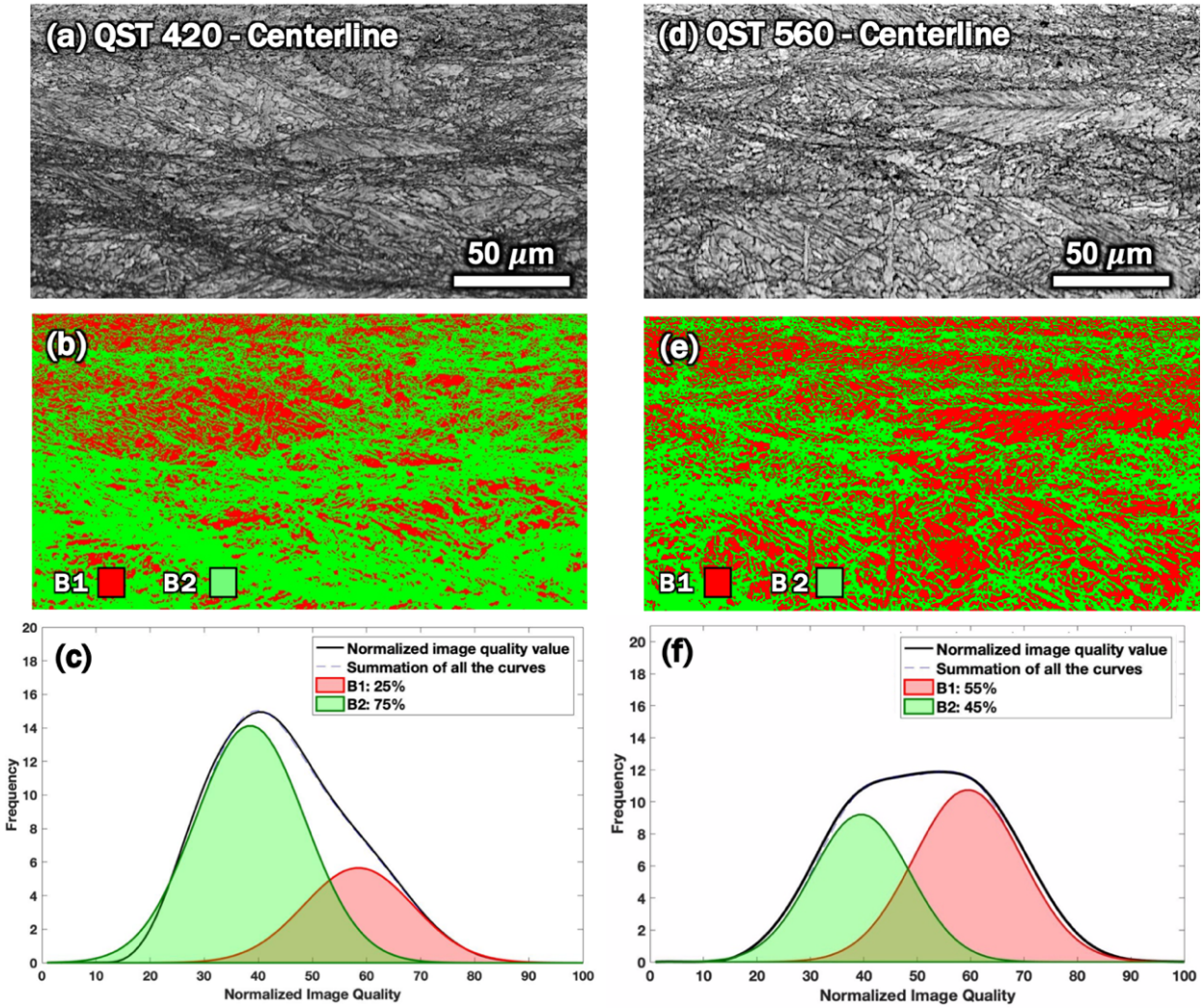

Figure 7 . Centerlines of RD-ND sections (Position II) for QST 420 in a) – c) and QST 560 in d) – f): a) and d) EBSD image quality, b) and e) location maps of identified microstructural components based on their IQ values, c) and f) normalized IQ distributions and fractions of each microstructural component.

3.2.Mechanical properties

3.2.1. Tensile properties

Fig. 8 shows the engineering stress-strain curves and corresponding strain hardening behavior of both QST 560 and QST 420 samples. Tensile curves revealed a continuous yielding behavior, which is very common in bainitic microstructures. The yield strength ($R_{p0.2}$) and ultimate tensile strength (R_m) of QST 420 were higher than those of QST 560. The high strength levels of QST 420 ($R_{p0.2}$ ~1270 MPa and R_m ~1410 MPa) gives a relatively high yield to ultimate strength ratio (~0.9) compared to the QST 560 (~0.78), which had almost 44 % and 36 % lower yield and tensile strengths, respectively. Accordingly, uniform elongation (A_g) and total elongation (A_t) values of QST 560 were higher than those of QST 420. Consequently, the total and uniform elongation that were achieved for QST 560 were ~19 % and ~8 %, i.e. respectively 1.3 and 2.3 times more than those for QST 420. The higher strength of QST

420 is primarily attributed to the presence of a higher fraction of the B2 morphology, which has a high density of dislocation networks and a higher fraction of high-angle boundaries as shown in Fig. 9.

A local Kernel average misorientation (KAM) map is an effective way to evaluate local strain concentrations and show the distribution of dislocation densities [30–32]. Fig. 10. shows the local strain concentration map with misorientation angles between 0° to 5° for both samples along with the relative frequency of each misorientation angle (Fig. 10(c)). In Fig. 10 (a-b), blue indicates a very low misorientation with less than 1°, green the angles in the range of 1° to 2°, yellow the angles 2° to 3°, and misorientation angles above 3° are indicated with red hues. Misorientations greater than 5° were not considered in the KAM evaluation as they interfere with low-angle grain boundaries. According to Fig. 10, the area with a misorientation of 1° was smaller in QST 420 than in QSR 560 and the area with higher misorientation angles was bigger indicating the presence of higher fractions with high-density dislocation networks [24] in QST 420 due to the presence of bainite type B2. This also accounts for the higher strength of QST 420 compared to QST 560.

The tensile true stress-strain curves were further analyzed to evaluate strain hardening behavior. The strain hardening rate ($d\sigma/d\varepsilon$) versus true strain (ε) for both samples are presented in Fig. 8(b). The strain hardening of the specimens started with the onset of yielding where the rate of strain hardening drops rapidly with initiation of strain in the same manner for both samples. Afterward, strain hardening rate decreased, but more slowly in QST 560 than QST 420, which consequently showed higher uniform elongation. Eventually, the strain hardening rate dropped sharply again in both samples most probably owing to the necking effect.

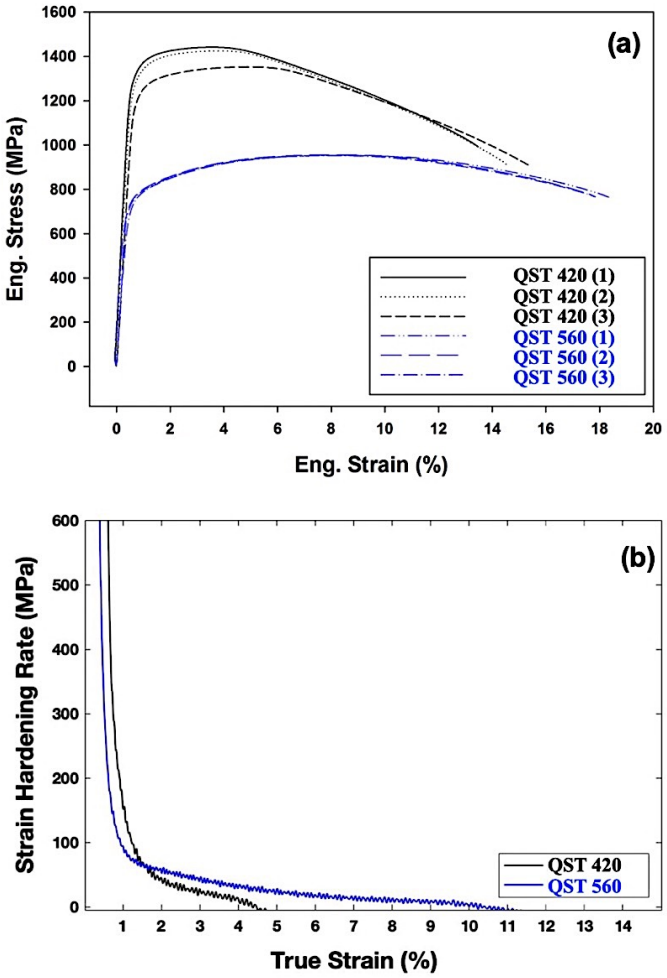

Figure 8. a) Engineering tensile stress-strain curves for the both samples and b) corresponding strain hardening rate.

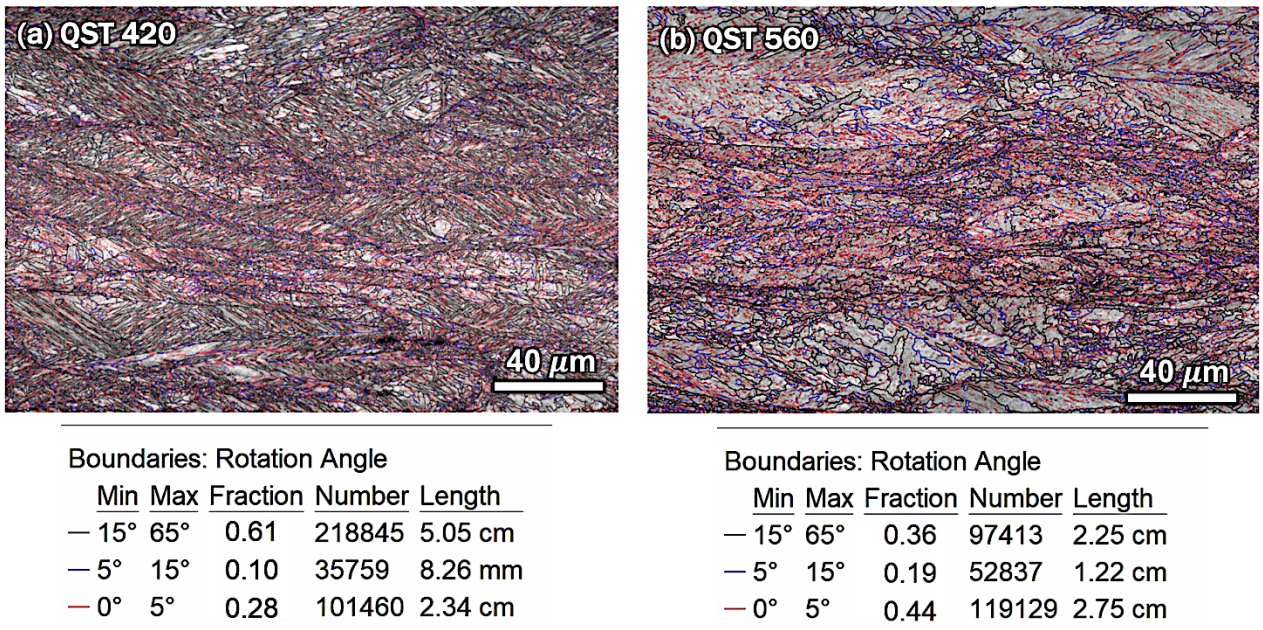

Boundaries: Rotation Angle

	Min	Max	Fraction	Number	Length
—	15°	65°	0.61	218845	5.05 cm
—	5°	15°	0.10	35759	8.26 mm
—	0°	5°	0.28	101460	2.34 cm

Boundaries: Rotation Angle

	Min	Max	Fraction	Number	Length
—	15°	65°	0.36	97413	2.25 cm
—	5°	15°	0.19	52837	1.22 cm
—	0°	5°	0.44	119129	2.75 cm

Figure 9. Grain boundary maps and the fractions of different misorientations for very low, low and high angle boundaries for a) QST 420 and b) QST 560 samples at centerline.

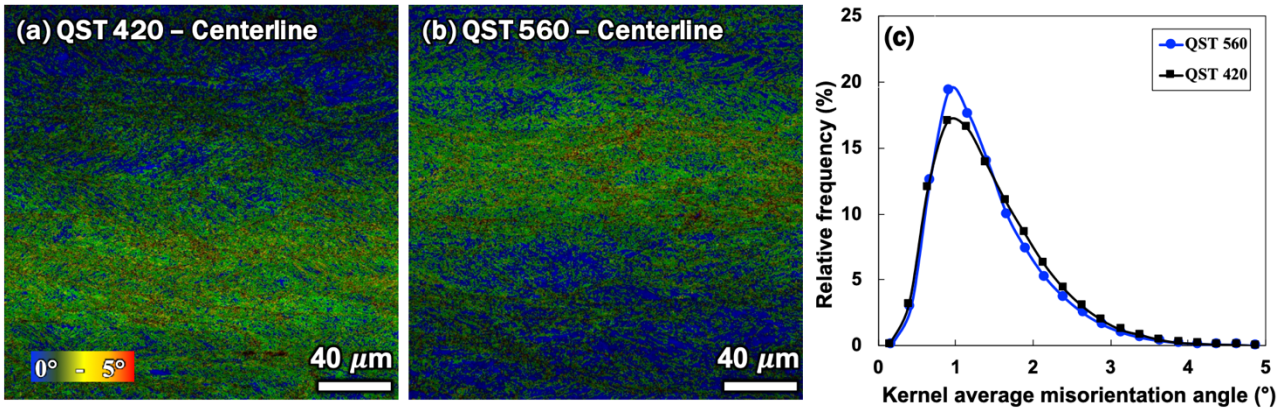

Figure 10. Kernel average misorientation maps for a) QST 420 and b) QST 560 samples at centerline along with c) the relative frequency of each misorientation angle.

3.2.2. Bending

Images of bent samples after three-point bending test using various punch radii are shown in Fig. 11. A precise visual macroscale inspection along with microscopic investigations on the surface and cross-section of damaged samples, i.e. cracked bent specimens and undamaged samples, revealed different types of surface defects caused by bending. Failure initiates near the bend axis by the formation and growth of surface waves parallel to the bend axis, and it later proceeds by the initiation and growth of subsurface cracks leading eventually to fracture on the convex surface when the strain is exceedingly localized due to a too small punch radius used. Following Kaupper and Merklein [33], the detected defects as well as the bendability acceptance criteria can be categorized using five different classes as schematically illustrated in Fig. 12. The schematic infograph, illustrating the type of defects as seen on the top surface of the bent sample (Fig.12 a) and on a central cross-section perpendicular to the bend axis (Fig.12 b), can also be used for understanding the damage development and failure mechanism on a macroscopic scale. The main damage zone broadens, and the severity of the defects increases from Class 1 to Class 5. To aid understanding, the FESEM micrographs given in Fig 12(c-d) show examples from Classes 2, 3 and 5 cross-section samples in QST 420 bent with a punch radius of 28 mm. Comparing macro and micro images, it can be seen that minor surface roughness or partial wavy structure were formed on the microscopic scale before they were obvious on the macro scale. More details about the failure and crack propagation will be discussed later in the fractography section.

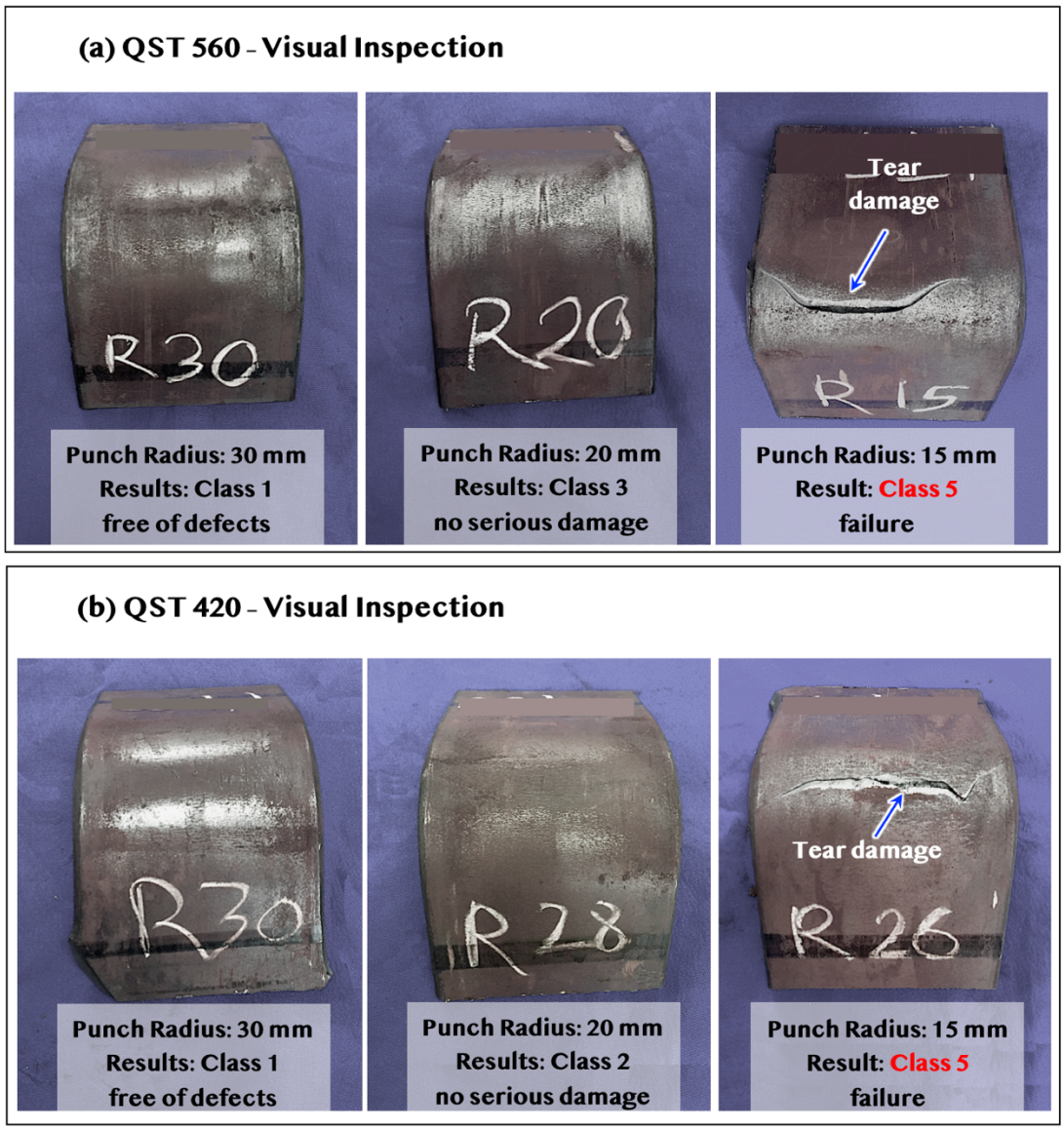

Figure 11. Images of the undamaged and damaged bent samples. a) QST 560 and b) QST 420. R_{XX} is the punch radius in mm.

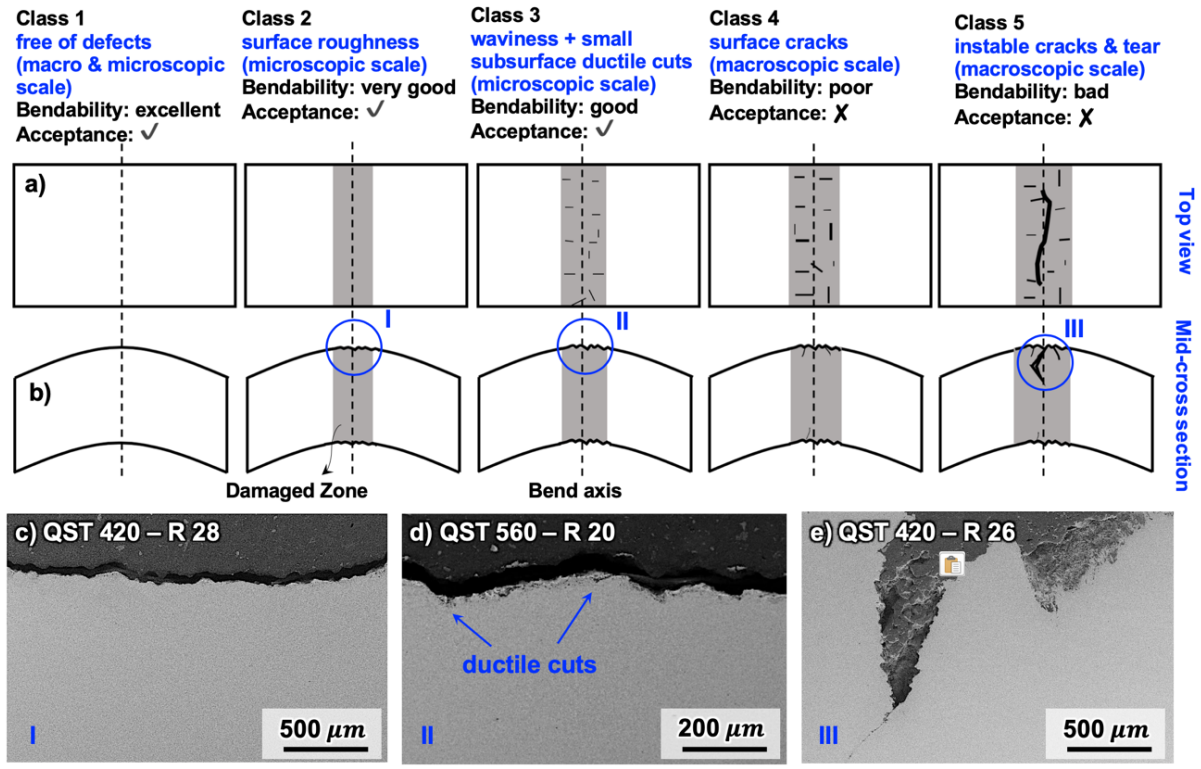

Figure 12. a) Schematic illustration of crack development during bending and different bendability classes on the basis of bent surface macro and micro inspections along with some actual microscopic examples for c) class 2, d) class 3 and e) class 5.

As there were no signs of any serious surface damage for QST 560 bent with a punch radius of 20 mm nor for QST 420 bent with a punch radius of 28 mm, the minimum usable ratio of punch radius (R) to sheet thickness (t) of 10 mm was 2.0 and 2.8 for QST 560 and 420, respectively. These ratios compare favorably with those of commercially available wear-resistant steels with similar tensile properties and levels of hardness. Table 1 summarizes the results for bending, hardness and tensile tests results as averages of three tests. The table also includes published data concerning two commercial industrial plates for comparison. Industrial example 1 has almost the same strength level as QST 560 and industrial example 2 has similar strength to QST 420. Despite the lack of satisfactory surface quality due to the laboratory rolling conditions and the use of as-rolled edges, both samples had almost 1.5 times better R/t ratios compared to the corresponding commercial materials. Of course, a large margin of safety has been included in the industrial values to allow for plate to plate variations, but still the difference is considerable.

Comparing the properties of the samples, QST 560 showed a better bendability by 30% due to its higher stain hardening rate (Fig. 10b) when compared to QST 420. Suppan et al. [1] showed that materials with higher strain hardening capability have better bendability as it leads to a more uniform strain distribution and thereby lesser formation of shear bands and notches. The higher fraction of the morphology (B1) with its low dislocation density in QST 560 improved its strain hardening capacity and increased its resistance against strain concentration during bending giving it enhanced bendability when compared to QST 420, which has a B2 bainitic morphology with a higher dislocation density. Sajjadi and Zebarjad [34] reported that the high strength of bainite formed at low temperature is due to the presence of a fine and uniform cementite distribution, a high dislocation density,

a high concentration of carbon dissolved in the bainitic ferrite, and higher internal stresses. Here, QST 420 showed a high fraction of high-angle grain boundaries as well. The distribution of microstructural components in QST 560 was fairly homogenous throughout the plate thickness, whereas the distribution of microstructural components in QST 420 depended on the distance from the rolling surface, such that subsurface regions consisted of a significant amount of hard martensite, which is detrimental to bendability.

Table 1. Hardness, bending and tensile properties (means of three tests and standard deviations) parallel to the RD of as-rolled samples and two commercial plates along with the ratio of upper to lower bainite for each parameter.

	QST 560	**QST 420**	**QST 560 / QST 420**	**Industrial plate Ex.1**	**Industrial plate Ex.2**
Yield strength, $R_{p0.2}$ [MPa]	711 ± 10	1267 ± 30	44% ¯	700	1200
Ultimate strength, R_m [MPa]	908 ± 11	1406 ± 28	36% ¯	1030	1400
Yield / Ultimate strength	0.78	0.90	13% ¯	0.68	0.86
Total elongation, A_t [%]	19.20 ± 0.20	14.70 ± 0.70	130% -	12	10
Uniform elongation, A_g [%]	7.80 ± 0.40	3.50 ± 0.5	223% -	Na	Na
Area under the curve [MPa]	158±1.5	185±2.0	15% ¯	Na	Na
Bulk mean hardness [HV10]	345 ± 6	425 ± 5	19% ¯	≥ 270	420-480
R/t (RD)	2.0	2.8	130% -	3 .0	4.5

3.2.3. Hardness

Through-thickness macrohardness distribution maps of undamaged bent plates as measured on central cross-sections are presented in Fig. 13(a). Fig. 13(b) shows an example of the source of the data in for QST 560 bent with a punch radius 20 mm. As each hardness indent affects the surrounding area within a certain radius, indentations were made with a minimum spacing of 1 mm. This still gave a sufficient number of indents across the thickness. In the presented example, the lowest hardness levels are marked in red for each hardness set and hot-rolled centerline is marked as a dashed line.

Excluding the surface layers of the samples, macrohardness decreases linearly from the surface down to the centerline in both samples from an average of 355 to 310 HV for QST 560 and from an average of 440 to 405 HV for the QST 420. In bending, the material is not strained to the same extent over the entire sample thickness, and as seen in Fig 13(a) the neutral axis, which at the start of bending is logically on the centerline, is shifted from the centerline toward the concave (inner) surface. This especially so in the QST 560 sample, which was bent with a smaller punch radius than the QST 420 sample shown.

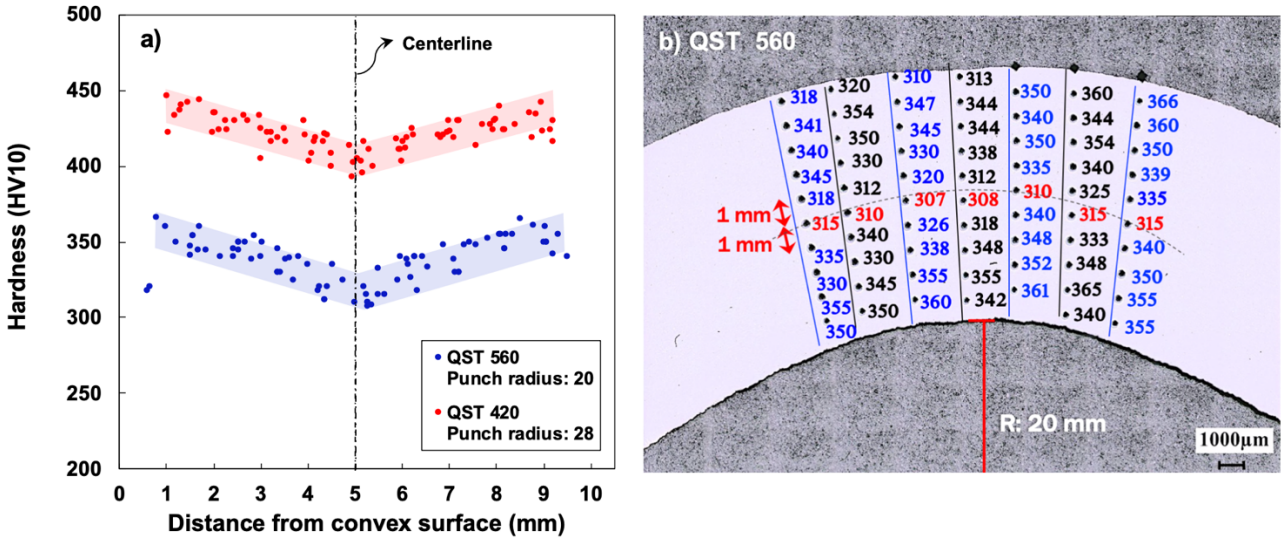

Figure 13. a) Through-thickness hardness distribution showing a shift of the neutral axis especially in QST 560. b) Hardness distribution through QST 560 bent with a punch radius of 20 mm.

3.3. Microtexture

EBSD inverse pole figure (IPF) data, acquired from areas of 200 x 200 μm^2 similar to Fig. 14 (a-b) and Fig. 15 (a-b) obtained from the centerline and subsurface of as-rolled samples, were used to calculate the orientation distribution function (ODF) maps in three-dimensional Euler space using OIM TSL software. The ODF results were used to evaluate the local texture of samples in the as-rolled (unbent) and bent conditions at different locations (Position I-VII). The major texture fibers and components in rolled body-centered cubic (bcc) materials, like the steel studied here, can be found in the two dimensional φ_2=45° section of Euler space. A schematic illustration of the ideal positions of bcc fibers and components in the φ_2=45° section under both shear and planar deformation is presented in Fig. 16.

Centerline ODF maps of as-rolled samples are illustrated in Fig. 14 (c and d). The texture of both samples was that typical of hot-rolled bands of carbon steel produced from pancaked austenite. Comparing the ODFs with Fig. 16, the general scheme of texture for both samples was similar comprising mainly ND (γ) and RD (α) fibers, with the main components $\{113\}\langle 110\rangle_\alpha$ and $\{112\}\langle 110\rangle_\alpha$ known as transformed copper, $\{111\}\langle 121\rangle_\alpha$ known as transformed brass, and $\{001\}\langle 110\rangle_\alpha$ known as rotated cube. The maximum intensity of the QST 420 sample was slightly higher compared to the QST 560. The texture intensity depends mainly on steel chemistry, amount of deformation, prior austenite grain shape and size, and also the cooling rate during transformation [35]. As all of the above parameters were maintained constant for both processing conditions except post-rolling cooling, it can be assumed that the slight increase in texture intensity in the lower bainite sample is due to its higher cooling rate.

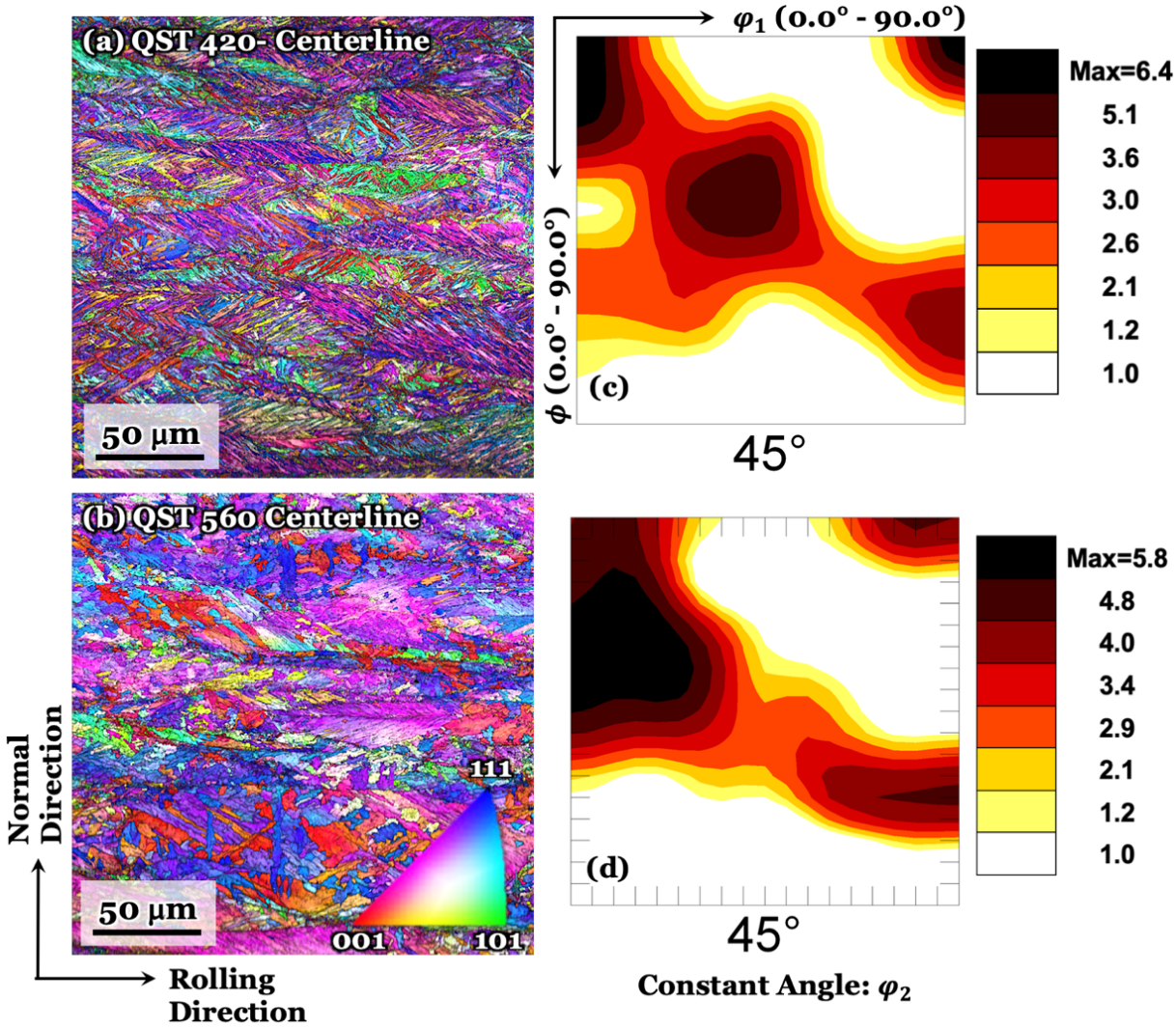

Figure 14. As-rolled centerline IPF and ODF map at φ_2= 45° of a) QST 420 and b) QST 560 obtained from an RD-ND section.

Fig. 15 shows the IPF and ODF maps at φ_2= 45° for the subsurface positions. A comparison of Fig. 15 and Fig. 16 shows that the strong bcc shear components $\{112\}\langle 111\rangle_\alpha$, $\{110\}\langle 112\rangle_\alpha$ and $\{110\}\langle 111\rangle_\alpha$ were observed in both samples. It has been reported [4,10] that since austenite is severely deformed by rolling below the RST, intense shear texture components $\{112\}\langle 110\rangle_\gamma$ and $\{111\}\langle 211\rangle_\gamma$ form in the austenite close to the rolled surfaces and later, during cooling, transform to the above-mentioned bcc shear components. However, the intensity of the cube component $\{001\}\langle 100\rangle_\alpha$, which is only observed in the samples close to the rolling surface, can be due to ferrite formation and its subsequent deformation by shearing during the rolling process [18]. As an example, IPF and ODF maps from close to the surface of an undamaged lower bainite sample bent with a punch radius of 28 mm is shown in Fig. 16. This specimen contained a significant amount of polygonal ferrite. As highlighted in Fig. 16(c), the $\{001\}\langle 100\rangle_\alpha$ orientation was formed mainly within the polygonal ferrite, which also showed a sharp shear component $\{110\}\langle 001\rangle_\alpha$, i.e. the Goss component. The possibility of microtexture evolution after bending was also studied. As there was no significant difference between overall textures before and after bending, the microstructures and textures are summarized in the appendix in Fig. 23 and Fig. 24.

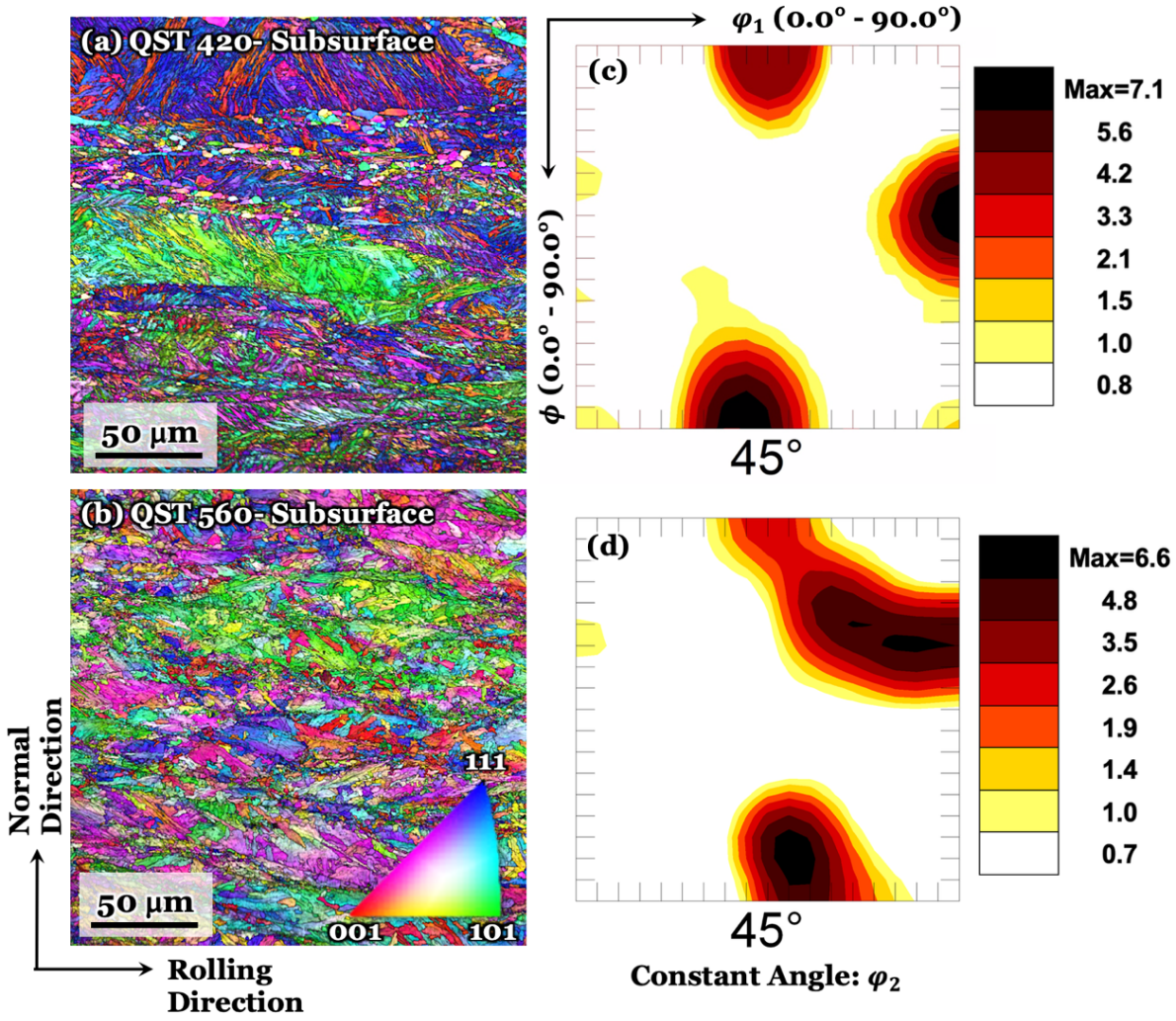

Figure 15. As-rolled subsurface IPF and ODF map at φ_2= 45° section of a) QST 420 and b) QST 560 obtained from an RD-ND section.

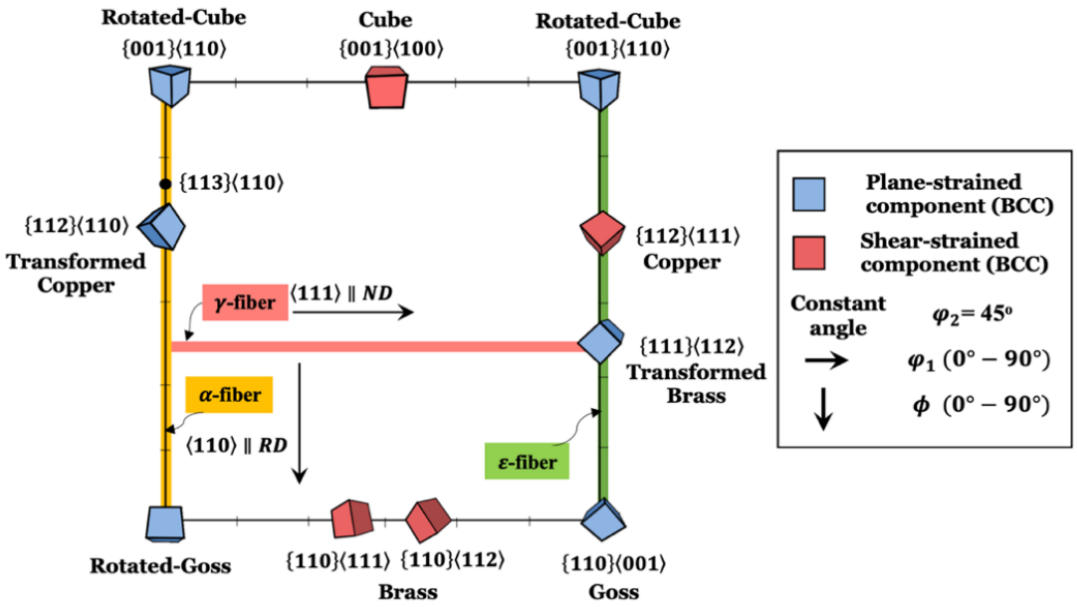

Figure 16. Illustration of ideal position of rolled bcc components and fibers an ODF map at φ_2= 45°.

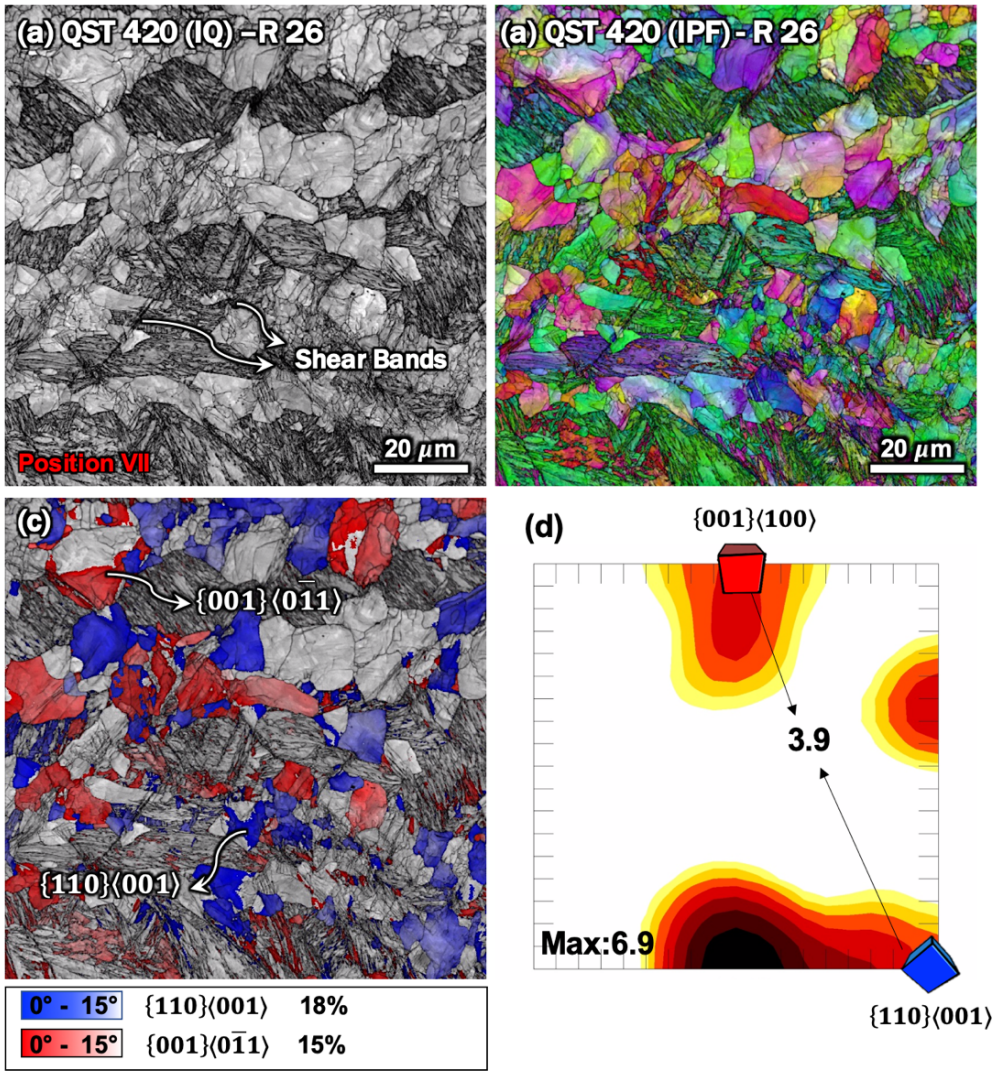

Figure 17. Exact concave surface microstructure and texture features of the lower bainite sample bent with a punch radius of 26 mm. a) Image quality indicating significant amount of polygonal ferrite and the formation of shear bands within the grains. b) Inverse pole figure map. c) Locations of the $\{110\}\langle001\rangle_{\alpha}$ and $\{110\}\langle001\rangle_{\alpha}$ components obtained with a tolerance angle of 15° from the ideal positions. d) Related ODF map at $\varphi_2 = 45°$ section.

3.4. Fractography

Damaged bent samples containing cracks were studied using FESEM-EBSD by examining unaltered fracture surfaces and polished and etched cross-sections of fracture surfaces to investigate the active fracture mechanisms. Fig. 18 presents fracture surfaces of damaged samples: QST 420 after bending with a punch radius of 26 mm in a) and b), and QST 560 bent with a 15 mm radius in c) and d). Two different fracture morphologies were observed in the region where failure initiated below the stretched outer convex surfaces.

The fracture surfaces of the QST 420 samples showed prior to brittle failure initiation stepwise crack propagation with alternating stretches of ductile multivoid-coalescence (MVC) and flat shearing (Fig. 18 a), which start from the stretched outer surface and end at the onset of continuous crack propagation. These flat steps are likely due to strain localization on areas with the highest critical resolved shear stress. On QST 560 there are less, and several times wider ridges present prior to brittle failure (Fig. 18 c) or they are completely absent. This is due to larger grains and continuous textural units of QST 560 as observed in Fig. 9 and Fig. 14 that enable easier accumulation of dislocations.

After brittle failure, QST 420 shows very shallow dimples with a bimodal size distribution (Fig. 18 b). On the other hand, post-failure fracture surfaces of QST 560 are very complex with a mix of locally cleaved facets, ductile MVC with deeper and coarser dimples, even some individual intergranular cracks and secondary cracks (Fig. 18 d), which are absent from QST 420. Generally, QST560 appears more ductile, which is in line with its tensile properties and bendability where the isothermal QST 560 microstructure had better elongation to fracture and forming capability (Table 1). No large non-metallic inclusions nor large voids could be linked to subsurface failure initiation in either material. Thus, inferior bendability of the lower bainitic material appears to be due to sensitivity to strain localization.

Cross-section of QST 420 outer convex surface layer, given in Fig. 19, shows that multiple parallel microcracks initiated at the tips of notches, and ductile cuts, where a number of small voids can be observed. According to Fig. 11 and Figs. 18-21, the damage process starts with strain localization followed by initiation and formation of shear bands within the grains (Fig. 17(a) and Fig. 24). Subsequently, depending on the surface strain and bending radius, it proceeds with roughening and development of surface waviness, which are followed by the nucleation of ductile tears and voids in the shear bands. Later, these voids grow, merge, and eventually develop into microcracks initiated from the surface valleys or subsurface ductile tears and cuts. The microcracks start to propagate and grow by shearing and merging into other cracks and voids to form the final fracture.

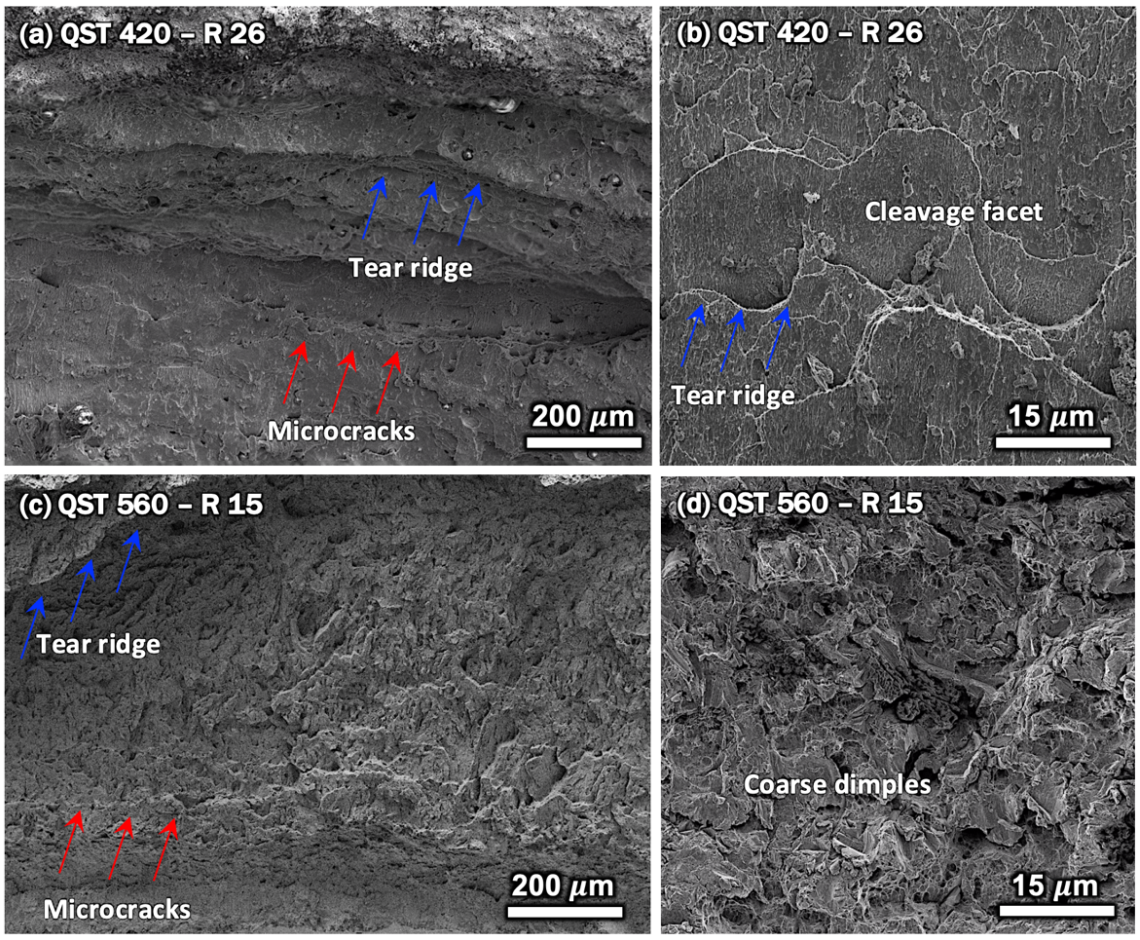

Figure 18. Fracture surfaces of damaged samples: a-b) QST 420 bent with a punch radius of 26 mm, and c-d) QST 560 bent with a punch radius of 15 mm.

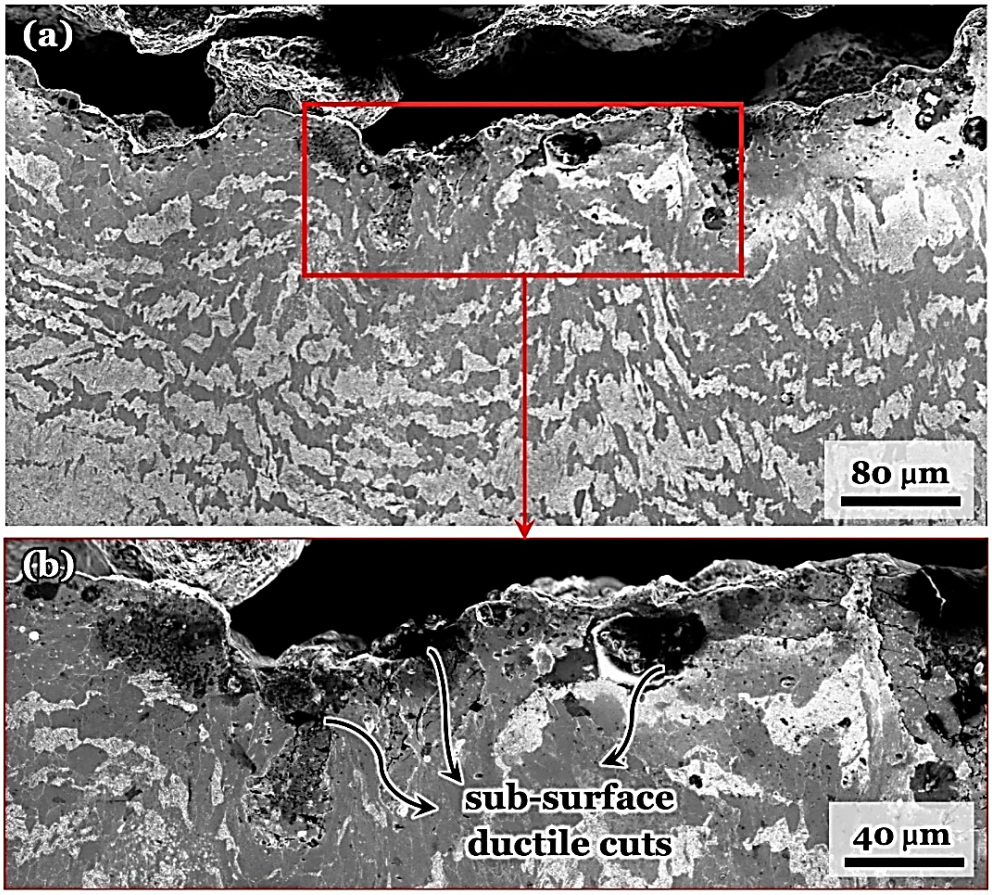

Figure 19. a) Cross-section through fracture surfaces of a damaged QST 420 sample. A higher magnification is given in b).

As shown in Fig. 20, the cracks propagated by shearing through the bainitic ferrite grains (blocks and packets) as well as through the prior austenite grains. Hence, the fracture appears to be transgranular. Thus, the refinement of both the prior austenite and final microstructures obstructs crack development and improve bendability. It has been also reported that a fine grain size can hinder surface roughness development at the outer convex surface as well, thereby decreasing the tendency for crack initiation at the surface [4] [2,5,8]. Mesarovic [36] showed that dislocations with certain Burgers vectors within a certain distance from the crack path are strongly attracted to the crack tip. Here, it is observed that crack propagates preferably through the region with higher strain and dislocation density i.e. B2 morphology.

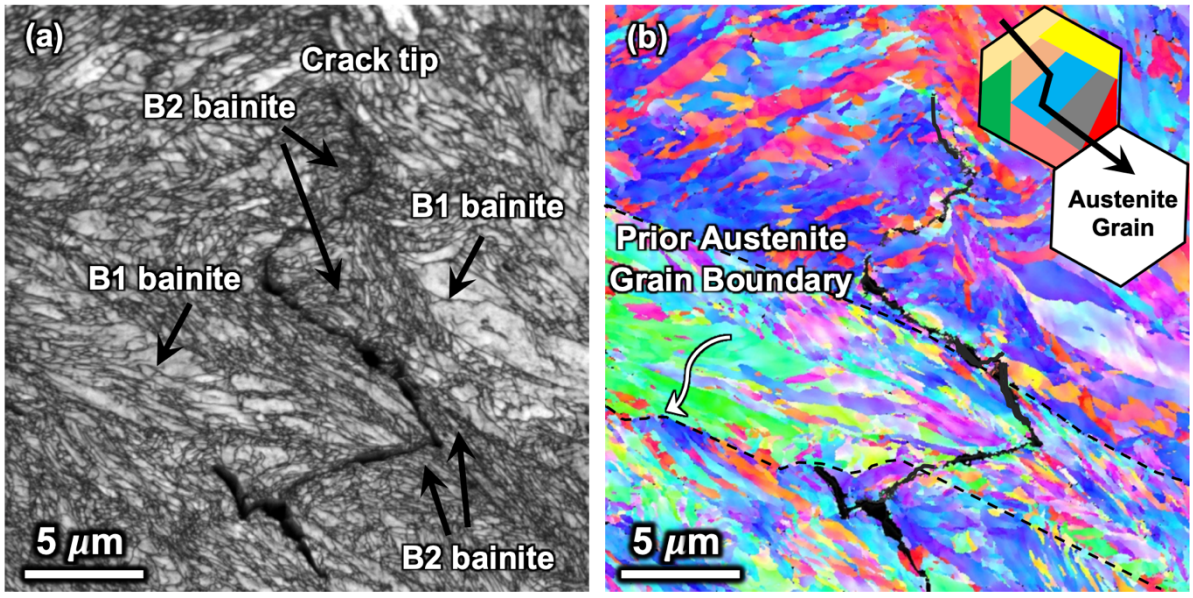

Figure 20. A crack path indicating that crack propagated through the region with the highest strain and highest dislocation density, i.e. B2 morphology, by a transgranular (both prior austenite and bainitic ferrite grains) fracture mechanism.

Regarding the effect of crystallographic texture on the bendability, and especially on the crack initiation and propagation, it has been widely reported that shear texture at the surface can have a detrimental on bendability, especially on crack initiation. For example, when the bend axis is transverse to the RD, strong shear texture components especially $\{110\}\langle 001\rangle_\alpha$ and $\{110\}\langle 112\rangle_\alpha$ brass components can promote shear localization, shear bands formation and surface roughness [9,18,37]. On the other hand, some planar rolling components can have beneficial effect on bendability by delaying the crack propagation. According to the Dillamore et al. [37] the presence of $\{112\}\langle 110\rangle_\alpha$ texture can prevent the propagation of shear bands. An example of a crack in a fractured lower bainite is presented in Fig. 21. Consistent with previous works [38,39], it is seen that grains with $\{001\}$ orientations, mainly the rotated cube component $\{001\}\langle 110\rangle_\alpha$, were more vulnerable to crack propagation. Also, as shown in Fig.21(b), there are two direction changes (marked as I and II) on the crack propagation path which happen when the crack reaches a $\{111\}\langle 121\rangle_\alpha$ component. Such observations are quite frequent indicating that this component can also hinder the crack propagation.

Fig. 22 shows the volume fraction of different texture components at the plate mid-thickness for both samples indicating the higher fraction of the detrimental component $\{001\}\langle 110\rangle_\alpha$ and the lower fraction of the beneficial components $\{112\}\langle 110\rangle_\alpha$ and $\{111\}\langle 121\rangle_\alpha$ in the QST 420 samples when compared to QST 560. The volume fraction of each component was calculated by considering a tolerance angle of 15° from the ideal position of each component.

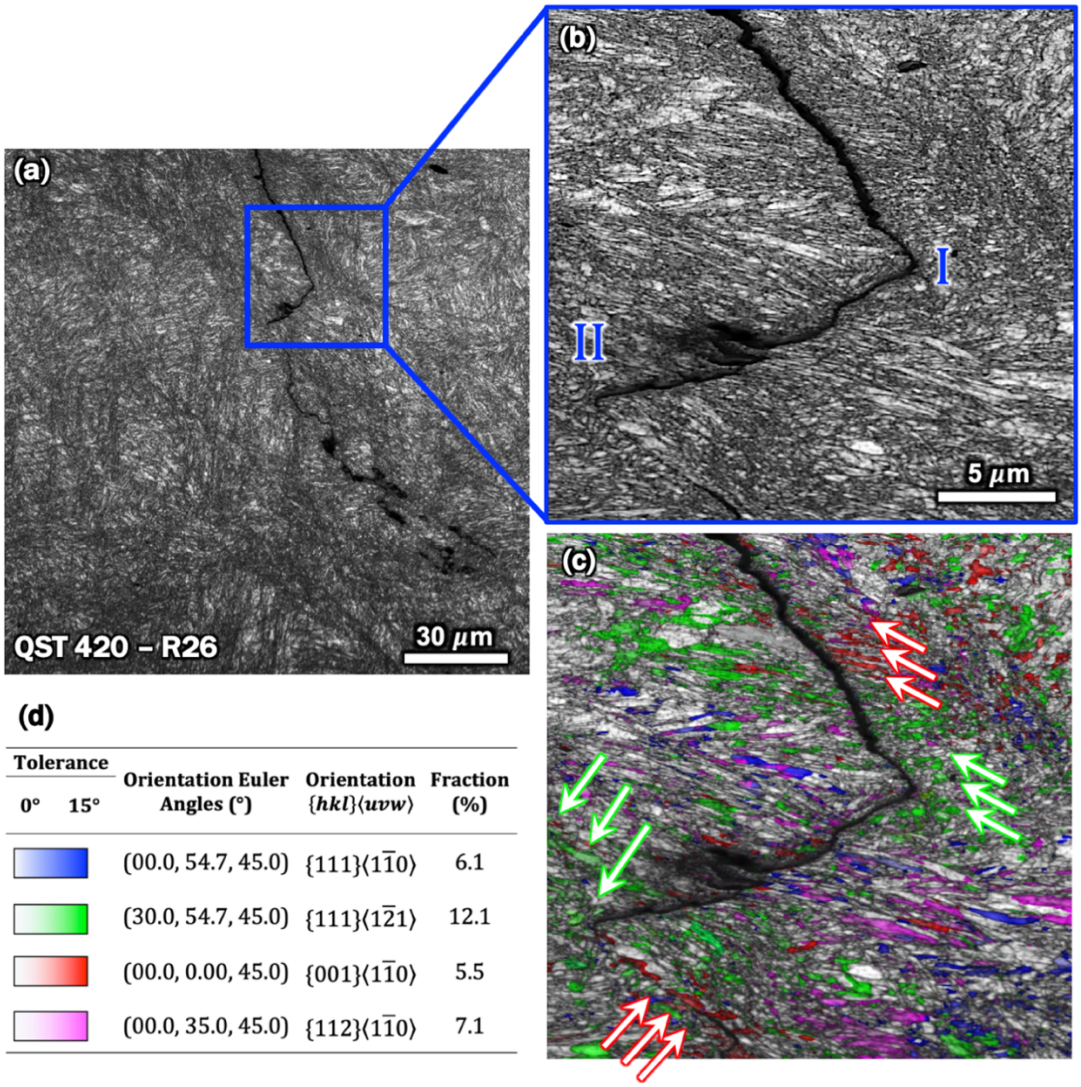

Tolerance 0°	Tolerance 15°	Orientation Euler Angles (°)	Orientation $\{hkl\}\langle uvw\rangle$	Fraction (%)
		(00.0, 54.7, 45.0)	$\{111\}\langle 1\bar{1}0\rangle$	6.1
		(30.0, 54.7, 45.0)	$\{111\}\langle 1\bar{2}1\rangle$	12.1
		(00.0, 0.00, 45.0)	$\{001\}\langle 1\bar{1}0\rangle$	5.5
		(00.0, 35.0, 45.0)	$\{112\}\langle 1\bar{1}0\rangle$	7.1

Figure 21. A crack path along with the textural component distribution map around the crack in a fractured QST 420 sample bent with a punch radius of 26 mm.

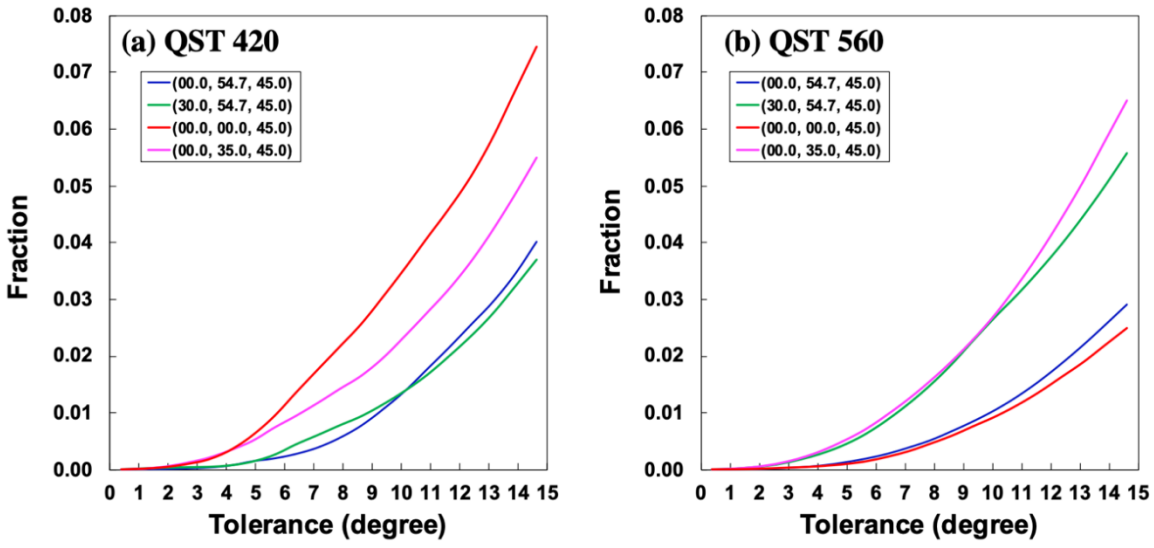

Figure 22. Volume fraction of texture components observed around cracks at the plate centerline, a) QST 420 and b) QST 560 samples.

Summarizing the factors affecting bendability, firstly, surface microstructure and texture affects the initiation of strain localization. For example, the formation of strong bcc shear components leads to pronounced shear band formation and surface roughness and waviness, which can promote the subsequent nucleation and growth of voids and microcracks. Also, the existence of soft microstructural constituents, like polygonal ferrite, at the surface can also delay strain localization and improve the bendability. Secondly, the cracks propagation affects by subsurface and the through-thickness microstructure and texture characteristics. Strain hardening capacity, which originate from microstructural features, significantly influence the bendability, the higher strain hardening capacity the better bendability. Work hardening can be increased by increasing the fraction of soft microstructural components with lower dislocation densities, like the B1 bainitic morphology, which delay the instability condition compared to the hard component with a high dislocation density, like B2 bainite and martensite. These results were in agreement with earlier work by Dillamore [37] which suggested that strain rate sensitivity, the work-hardening exponent, the density of mobile dislocations were the main parameters that affect the bendability of heavily deformed material.

4. Conclusion

The bendability of a new steel composition in the as-rolled state with two different post rolling cooling conditions was investigated using three-point bending tests. The different QST temperature led to formation of different quantity of microstructural components in the samples, resulting different mechanical and bending properties. The sample with a quench stop temperature of 560 °C had a lower strength level but higher strain hardening capacity than the one with a QST of 420 °C, which led to a better bendability (R/t = 2) in QST 560 compared to QST 420 (R/t = 2.8). For QST 560, bending with punch radii smaller than 2t led to ductile fracture while QST 420 bent with radii smaller than 2.8t tended to show more brittle fracture appearance. Compared to commercially available steel grades with similar mechanical properties, both samples showed very good minimum usable R/t ratios already in the lab-made condition and as-rolled edges. The bending tests revealed that, irrespective of the strength level, bendability would not be an issue when forming this steel, for example to wear-resistant pipes for slurry transportation. The main conclusions can be highlighted as follows:

- Irrespective of QST, the microstructure down to a depth of about 100 μm from the surface consisted of a significant fraction of polygonal ferrite scattered among the carbon-rich microstructural components martensite and bainite.
- The effect of QST on tensile strength is due to changes in the fractions of the microstructural constituents and not to other parameters crystallographic texture, grain size.
- From the crack propagation viewpoint, formation of lower fraction of the detrimental component $\{001\}\langle 110\rangle_{\alpha}$ and the higher fraction of the beneficial components $\{112\}\langle 110\rangle_{\alpha}$ and $\{111\}\langle 121\rangle_{\alpha}$ in the QST 560 samples when compared to QST 420 helped QST 560 samples to show a better bending behavior.
- The bendability of the studied materials with the bend axis transverse to the rolling direction was mainly affected by strain hardening capacity, crystallographic surface and through thickness characteristics, and the distribution of microstructural components.
- There was no evidence of microtexture evolution after bending through the samples thickness.

CRediT authorship contribution statement

Vahid Javaheri: Writing - original draft, Formal analysis, Investigation, Resources, Visualization, Data curation, Conceptualization. **Sakari Pallaspuro:** Formal analysis, Review & editing. **Antti Kaijalainen:** Review & editing, **Saeed Sadeghpour:** Formal analysis, Visualization, Review & editing. **Jukka Kömi:** Project administration, Supervision. **David Porter:** Conceptualization, Review & editing, Supervision.

Acknowledgment

The authors are grateful for financial support from the Academy of Finland (#311934 – Genome of Steel Project). Vahid Javaheri would also like to thank the Jenny and Antti Wihuri Foundation for a personal grant.

Data Availability

The raw/processed data required to reproduce these findings cannot be shared at this time as the data also forms part of an ongoing study but will be made available on request.

Reference

[1] C. Suppan, T. Hebesberger, A. Pichler, J. Rehrl, O. Kolednik, On the microstructure control of the bendability of advanced high strength steels, Mater. Sci. Eng. A. 735 (2018) 89–98. https://doi.org/10.1016/j.msea.2018.07.080.

[2] A. Davidkov, M.K. Jain, R.H. Petrov, D.S. Wilkinson, R.K. Mishra, Strain localization and damage development during bending of Al-Mg alloy sheets, Mater. Sci. Eng. A. 550 (2012) 395–407. https://doi.org/10.1016/j.msea.2012.04.093.

[3] A.J. Kaijalainen, P. Suikkanen, L.P. Karjalainen, J.J. Jonas, Effect of Austenite pancaking on the microstructure, texture, and bendability of an ultrahigh-strength strip steel, Metall. Mater. Trans. A Phys. Metall. Mater. Sci. 45 (2014) 1273–1283. https://doi.org/10.1007/s11661-013-2062-7.

[4] A.J. Kaijalainen, M. Liimatainen, V. Kesti, J. Heikkala, T. Liimatainen, D.A. Porter, Influence of Composition and Hot Rolling on the Subsurface Microstructure and Bendability of Ultrahigh-Strength Strip, Metall. Mater. Trans. A Phys. Metall. Mater. Sci. 47 (2016) 4175–4188. https://doi.org/10.1007/s11661-016-3574-8.

[5] N. Pornputsiri, K. Kanlayasiri, Effect of bending temperatures on the microstructure and springback of a TRIP steel sheet, Def. Technol. (2019). https://doi.org/10.1016/j.dt.2019.11.018.

[6] S.K. Hazra, P. Efthymiadis, A. Alamoudi, R.L.V. Kumar, B. Shollock, R. Dashwood, The bendability of ultra high strength steels, J. Phys. Conf. Ser. 734 (2016). https://doi.org/10.1088/1742-6596/734/3/032097.

[7] M.S. Joo, D.W. Suh, J.H. Bae, N. Sanchez Mouriño, R. Petrov, L.A.I. Kestens, H.K.D.H. Bhadeshia, Experiments to separate the effect of texture on anisotropy of pipeline steel, Mater. Sci. Eng. A. 556 (2012) 601–606. https://doi.org/10.1016/j.msea.2012.07.033.

[8] D. Rèche, T. Sturel, O. Bouaziz, A. Col, A.F. Gourgues-Lorenzon, Damage development in low alloy TRIP-aided steels during air-bending, Mater. Sci. Eng. A. 528 (2011) 5241–5250. https://doi.org/10.1016/j.msea.2011.03.042.

[9] A. Saastamoinen, A. Kaijalainen, J. Heikkala, D. Porter, P. Suikkanen, The effect of tempering temperature on microstructure, mechanical properties and bendability of direct-quenched low-alloy strip steel, Mater. Sci. Eng. A. 730 (2018) 284–294. https://doi.org/10.1016/j.msea.2018.06.014.

[10] A. Saastamoinen, A. Kaijalainen, D. Porter, P. Suikkanen, The effect of thermomechanical treatment and tempering on the subsurface microstructure and bendability of direct-quenched low-carbon strip steel, Mater. Charact. 134 (2017) 172–181. https://doi.org/10.1016/j.matchar.2017.10.020.
[11] R. Roumina, M. Bruhis, J.P. Masse, H.S. Zurob, M. Jain, O. Bouaziz, J.D. Embury, Bending properties of functionally graded 300M steels, Mater. Sci. Eng. A. 653 (2016) 63–70. https://doi.org/10.1016/j.msea.2015.12.012.
[12] P.J. Jacques, Q. Furnémont, F. Lani, T. Pardoen, F. Delannay, Multiscale mechanics of TRIP-assisted multiphase steels: I. Characterization and mechanical testing, Acta Mater. 55 (2007) 3681–3693. https://doi.org/10.1016/j.actamat.2007.02.029.
[13] M. Azuma, S. Goutianos, N. Hansen, G. Winther, X. Huang, Effect of hardness of martensite and ferrite on void formation in dual phase steel, Mater. Sci. Technol. 28 (2012) 1092–1100. https://doi.org/10.1179/1743284712Y.0000000006.
[14] T. Matsuno, D. Maeda, H. Shutoh, A. Uenishi, M. Suehiro, Effect of Martensite Volume Fraction on Void Formation Leading to Ductile Fracture in Dual Phase Steels, ISIJ Int. 54 (2014) 938–944. https://doi.org/10.2355/isijinternational.54.938.
[15] D. Raabe, K. Lücke, Texture and microstructure of hot rolled steel, Scr. Metall. Mater. 26 (1992) 1221–1226. https://doi.org/10.1016/0956-716X(92)90567-X.
[16] M.S. Joo, D.-W. Suh, J.H. Bae, H.K.D.H. Bhadeshia, Role of delamination and crystallography on anisotropy of Charpy toughness in API-X80 steel, Mater. Sci. Eng. A. 546 (2012) 314–322. https://doi.org/10.1016/j.msea.2012.03.079.
[17] R. Esterl, M. Sonnleitner, I. Weißensteiner, K. Hartl, R. Schnitzer, Influence of quenching conditions on texture and mechanical properties of ultra-high-strength steels, J. Mater. Sci. 54 (2019) 12875–12886. https://doi.org/10.1007/s10853-019-03787-z.
[18] A.J. Kaijalainen, M. Liimatainen, V. Kesti, J. Heikkala, T. Liimatainen, D.A. Porter, Influence of Composition and Hot Rolling on the Subsurface Microstructure and Bendability of Ultrahigh-Strength Strip, Metall. Mater. Trans. A Phys. Metall. Mater. Sci. 47 (2016) 4175–4188. https://doi.org/10.1007/s11661-016-3574-8.
[19] V. Javaheri, N. Khodaie, A. Kaijalainen, D. Porter, Effect of niobium and phase transformation temperature on the microstructure and texture of a novel 0.40% C thermomechanically processed steel, Mater. Charact. 142 (2018) 295–308. https://doi.org/10.1016/j.matchar.2018.05.056.
[20] V. Javaheri, T. Nyyssönen, B. Grande, D. Porter, Computational Design of a Novel Medium-Carbon, Low-Alloy Steel Microalloyed with Niobium, J. Mater. Eng. Perform. (2018). https://doi.org/10.1007/s11665-018-3376-9.
[21] V. Javaheri, A. Pohjonen, J.I. Asperheim, D. Ivanov, D. Porter, Physically based modeling, characterization and design of an induction hardening process for a new slurry pipeline steel, Mater. Des. 182 (2019) 108047. https://doi.org/10.1016/j.matdes.2019.108047.
[22] A.J. DeArdo, C.I. Garcia, K. Cho, M. Hua, New method of characterizing and quantifying complex microstructures in steels, Mater. Manuf. Process. 25 (2010) 33–40. https://doi.org/10.1080/10426910903143415.
[23] J. Wu, P.J. Wray, C.I. Garcia, M. Hua, A.J. Deardo, Image quality analysis: A new method of characterizing microstructures, ISIJ Int. 45 (2005) 254–262. https://doi.org/10.2355/isijinternational.45.254.
[24] T. Zhou, H. Yu, J. Hu, S. Wang, Study of microstructural evolution and strength-toughness mechanism of heavy-wall induction bend pipe, Mater. Sci. Eng. A. 615 (2014) 436–446. https://doi.org/10.1016/j.msea.2014.07.101.
[25] H.K.D.H. Bhadeshia, Bainite in Steels, Transformation, Microstructure and Properties, Second, IOM Comminucations Ltd, 2011.
[26] T. Song, B.C. De Cooman, Effect of Boron on the Isothermal Bainite Transformation,

Metall. Mater. Trans. A. 44 (2013) 1686–1705. https://doi.org/10.1007/s11661-012-1522-9.
[27] S.I. Wright, M.M. Nowell, EBSD Image Quality Mapping, Microsc. Microanal. 12 (2006) 72–84. https://doi.org/10.1017/S1431927606060090.
[28] X. Tao, A. Eades, Alternatives to Image Quality (IQ) Mapping in EBSD, Microsc. Microanal. 8 (2002) 692–693. https://doi.org/10.1017/S1431927602106465.
[29] A.J. DeArdo, M.J. Hua, K.G. Cho, C.I. Garcia, On strength of microalloyed steels: an interpretive review, Mater. Sci. Technol. 25 (2009) 1074–1082. https://doi.org/10.1179/174328409X455233.
[30] E.P. Kwon, S. Fujieda, K. Shinoda, S. Suzuki, Characterization of transformed and deformed microstructures in transformation induced plasticity steels using electron backscattering diffraction, Mater. Sci. Eng. A. 528 (2011) 5007–5017. https://doi.org/10.1016/j.msea.2011.03.033.
[31] D. De Knijf, R. Petrov, C. Föjer, L.A.I. Kestens, Effect of fresh martensite on the stability of retained austenite in quenching and partitioning steel, Mater. Sci. Eng. A. 615 (2014) 107–115. https://doi.org/10.1016/j.msea.2014.07.054.
[32] J. Sun, H. Yu, S. Wang, Y. Fan, Study of microstructural evolution, microstructure-mechanical properties correlation and collaborative deformation-transformation behavior of quenching and partitioning (Q&P) steel, Mater. Sci. Eng. A. 596 (2014) 89–97. https://doi.org/10.1016/j.msea.2013.12.054.
[33] M. Kaupper, M. Merklein, Bendability of advanced high strength steels—A new evaluation procedure, CIRP Ann. 62 (2013) 247–250. https://doi.org/10.1016/j.cirp.2013.03.049.
[34] S.A. Sajjadi, S.M. Zebarjad, Isothermal transformation of austenite to bainite in high carbon steels, J. Mater. Process. Technol. 189 (2007) 107–113. https://doi.org/10.1016/j.jmatprotec.2007.01.011.
[35] R.K. Ray, J.J. Jonas, M.P. Burton-Guillen, J. Savoie, Transformation textures in steels, ISIJ Int. 34 (1994) 972–942.
[36] S. Mesarovic, The influence of pre-existing dislocations on cleavage crack propagation behavior in crystals, J. Mech. Phys. Solids. 45 (1997) 211–223. https://doi.org/10.1016/S0022-5096(96)00079-8.
[37] I.L. Dillamore, J.G. Roberts, A.C. Bush, Occurrence of shear bands in heavily rolled cubic metals, Met. Sci. 13 (1979) 73–77. https://doi.org/10.1179/msc.1979.13.2.73.
[38] R. Joodaki, S.R. Alavi Zaree, K. Gheisari, M. Eskandari, Effect of Annealing Treatments on the Microstructure and Texture Development in API 5L X60 Microalloyed Pipeline Steel, J. Mater. Eng. Perform. 26 (2017) 2003–2013. https://doi.org/10.1007/s11665-017-2673-z.
[39] J.I. Verdeja, J. Asensio, J.A. Pero-Sanz, Texture, formability, lamellar tearing and HIC susceptibility of ferritic and low-carbon HSLA steels, Mater. Charact. 50 (2003) 81–86. https://doi.org/10.1016/S1044-5803(03)00106-2.

Appendix

The microstructure and texture details of both QST 420 and QST 460 before and after bending is summarized in Fig. 23 and Fig, 24.

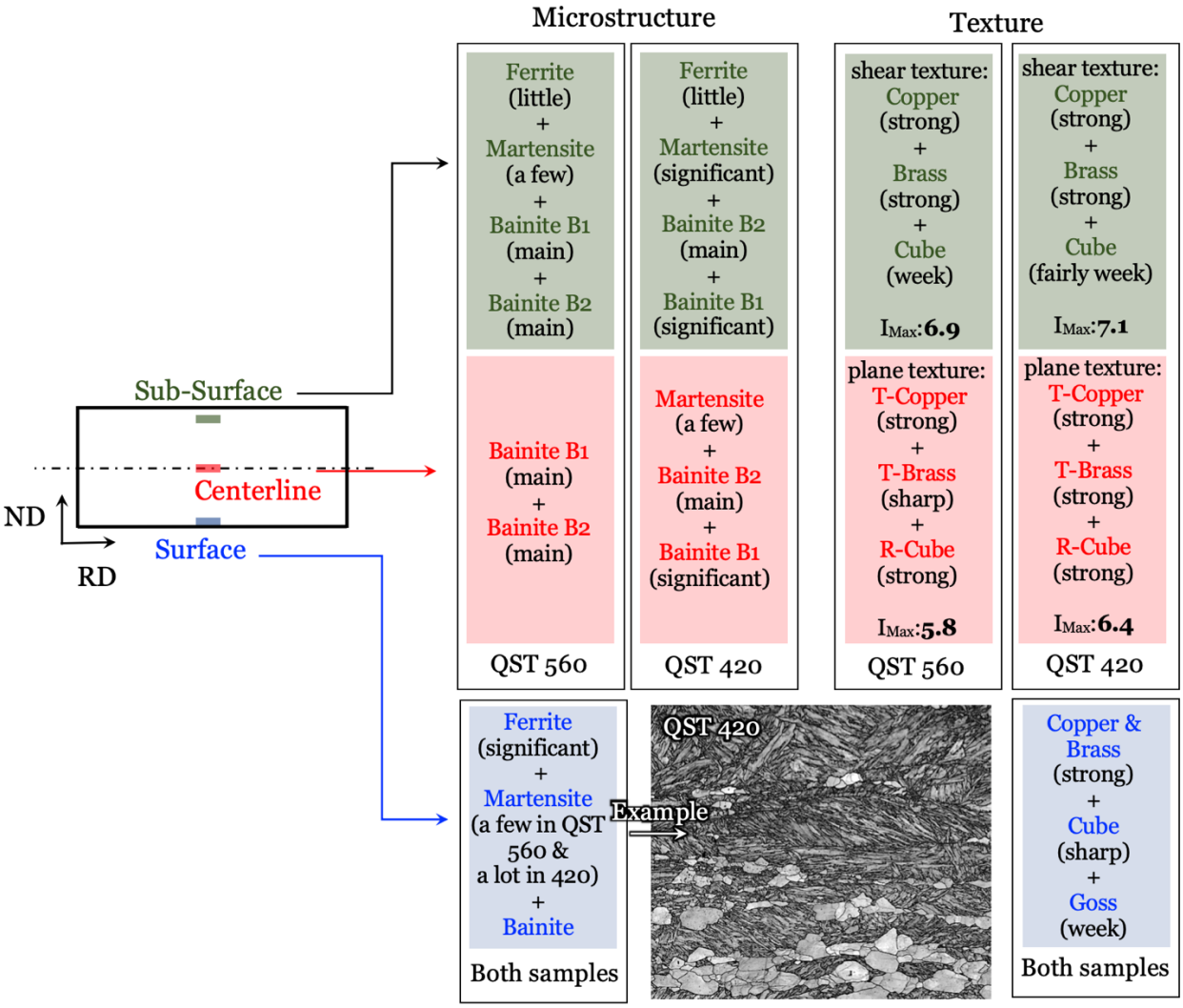

Figure 23. As-rolled texture and microstructures of both samples at the different positions of surface, subsurface and mid-thickness.

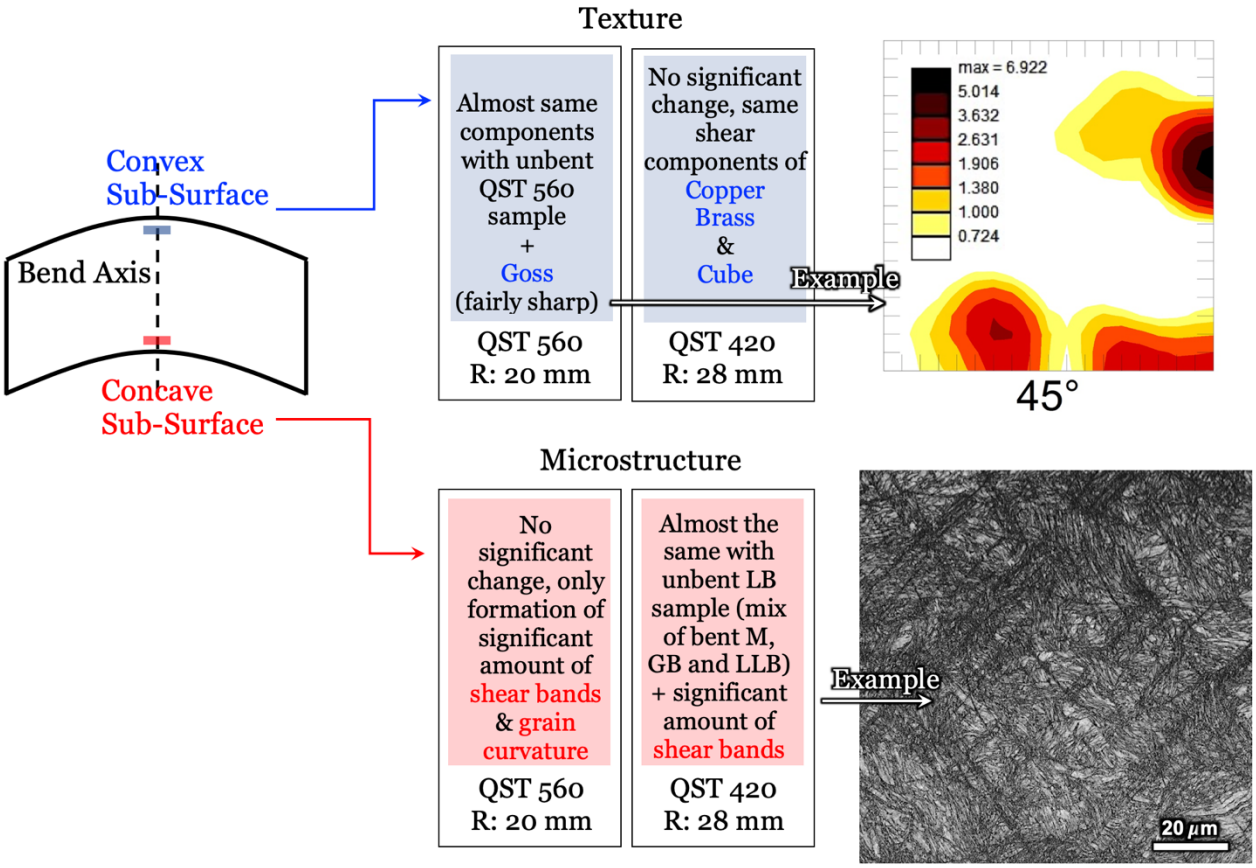

Figure 24. Texture and microstructure of both samples after bending at the convex and concave sub surfaces.